1 **Nitrate Chemistry in the Northeast US Part II: Oxygen Isotopes Reveal**

2 **Differences in Particulate and Gas Phase Formation**

3 Heejeong Kim[1,2*], Wendell W. Walters[2*], Claire Bekker[1, a], Lee T. Murray[3], and Meredith G.

4 Hastings[1,2]

5 [1]Department of Earth, Environmental, and Planetary Sciences, Brown University; Providence, RI 02912, USA.

6 [2]Institute at Brown for Environment and Society, Brown University; Providence, RI 02912, USA

7 [3]Department of Earth and Environmental Sciences, University of Rochester; Rochester, NY 14627, USA

8 [a]Now at Environmental Health Sciences, University of California Los Angeles; Los Angeles, CA 90095

10 *Correspondence to*:

11 Heejeong Kim (heejeong_kim@brown.edu)

12 Wendell W. Walters (wendell_walters@brown.edu)

14 **Abstract.** The northeastern US represents a mostly urban corridor impacted by high population

15 and fossil-fuel combustion emission density. This has led to historically degraded air quality and

16 acid rain that has been a focus of regulatory-driven emissions reductions. Detailing the chemistry

17 of atmospheric nitrate formation is critical for improving the model representation of atmospheric

18 chemistry and air quality. The oxygen isotopic composition of atmospheric nitrate are useful

19 indicators in tracking nitrate formation pathways. Here, we measured oxygen isotope deltas ($\Delta(^{17}O)$

20 and $\delta(^{18}O)$) for nitric acid (HNO_3) and particulate nitrate (pNO_3) from three US EPA Clean Air

21 Status and Trends Network (CASTNET) sites in the northeastern US from December 2016 to 2018.

22 The $\Delta(^{17}O, HNO_3)$ and $\delta(^{18}O, HNO_3)$ values ranged from 12.9 ‰ to 30.9 ‰ and from 46.9 ‰ to

23 82.1 ‰, and the $\Delta(^{17}O, pNO_3)$ and $\delta(^{18}O, pNO_3)$ ranged from 16.6 ‰ to 33.7 ‰ and from 43.6 ‰

24 to 85.3 ‰, respectively. There was distinct seasonality of $\delta(^{18}O)$ and $\Delta(^{17}O)$ with higher values

25 observed during winter compared to summer, suggesting a shift in O_3 to HO_x radical chemistry, as

26 expected. Unexpectedly, there was a statistical difference in $\Delta(^{17}O)$ between HNO_3 and pNO_3, with

27 higher values observed for pNO$_3$ (27.1±3.8) ‰ relative to HNO$_3$ (22.7±3.6) ‰, and significant

28 differences in the relationship between $\delta(^{18}O)$ and $\Delta(^{17}O)$. This difference suggests atmospheric

29 nitrate phase-dependent oxidation chemistry that is not predicted in models. Based on the output

30 from GEOS-Chem, and both the $\delta(^{18}O)$ and $\Delta(^{17}O)$ observations, we quantify the production

31 pathways of atmospheric nitrate. The model significantly overestimated the heterogeneous N$_2$O$_5$

32 hydrolysis production for both HNO$_3$ and pNO$_3$, a finding consistent with observed seasonal

33 changes in $\delta(^{18}O)$ and $\Delta(^{17}O)$ of HNO$_3$ and pNO$_3$, though large uncertainties remain in the

34 quantitative transfer of $\delta(^{18}O)$ from major atmospheric oxidants. This comparison provides

35 important insight into the role of oxidation chemistry in reconciling a commonly observed positive

36 bias for modeled atmospheric nitrate concentrations in the northeastern US.

1. Introduction

39 Nitrogen oxides (NO$_x$ = NO + NO$_2$) in the atmosphere have an important impact on air quality and

40 human and ecosystem health (Galloway et al., 2004). NO$_x$ plays an important role in influencing

41 the oxidizing efficiency of the atmosphere, including the production of ozone (O$_3$), and leads to

42 the formation of atmospheric nitrate (gas phase nitric acid (HNO$_3$) and nitrate in particulate form

43 (pNO$_3$)) (Crutzen et al., 1979). HNO$_3$ and pNO$_3$ are, in turn, important contributors to dry and wet

44 N deposition. Nitrate is a key component of particulate matter (PM$_{2.5}$), which has direct adverse

45 effects on human respiratory and climate change, and the deposition of N to ecosystems can

46 contribute to soil acidification and eutrophication (Camargo and Alonso, 2006; Schlesinger, 2007;

47 Tai et al., 2010). Thus, changes in the chemistry and chemical feedbacks associated with NO$_x$ have

48 important implications for predicting air quality improvements and climatic responses.

49

50 The US Environmental Protection Agency (EPA) reported that NO$_x$ emissions have decreased by

51 36 % in the United States from 2007 to 2015 due to effective regulations in response to the Clean

52 Air Act and its Amendments (US EPA, 2017; CASTNET, 2019; NEI, 2017; Shah et al., 2018).

53 However, atmospheric pNO$_3$ concentrations have responded sub-linearly to the dramatic NO$_x$

54 emission reductions, with only a 7.8 % pNO$_3$ decrease over the same period in the northeastern

55 US. Uncertainties in our understanding between NO$_x$ reductions and the production of atmospheric

56 nitrate challenge our ability to make effective reductions in reactive nitrogen concentrations. Major

57 factors influencing atmospheric nitrate production include oxidant availability, heterogeneous

58 chemistry, gas-to-particle partitioning, and potential aerosol nitrate photolysis (Jaeglé et al., 2018;

59 Shah et al., 2018; Kasibhatla et al., 2018).

60

61 Atmospheric nitrate concentrations have been simulated using various chemistry models to detail

62 spatiotemporal variabilities between precursor NO_x emissions and nitrate in the US, with

63 somewhat limited success (Walker et al., 2012; Zhang et al., 2012). In particular, the

64 concentrations of nitrate observed in the northeastern US tend to be overestimated in models (e.g.,

65 Heald et al., 2012; Zhang et al., 2012), which is an important region to monitor due to its high

66 population density, transport patterns and the tendency for poor air quality (Sickles and Shadwick,

67 2015). Modeling studies suggest that biases revealed by comparison with observations could be

68 due to uncertainties in NO_x and gaseous ammonia (NH_3) emission estimates, dry deposition

69 removal rates, heterogeneous chemical production rates, and changing chemistry due to reductions

70 in NO_x and sulfur dioxide emissions (Heald et al., 2012; Holt et al., 2015; Shah et al., 2018).

71

72 The nitrate oxygen isotope deltas ($\Delta(^{17}O)$ and $\delta(^{18}O)$) have proven to provide observational

73 constraints on the oxidation pathways that are responsible for the formation of atmospheric nitrate

74 (Hastings et al., 2003; Michalski et al., 2003; Alexander et al., 2009). The isotopic composition is

75 expressed as δ, which is a standardized notation and quantified as $\delta = (R_{sample}/R_{reference} - 1)$. R is

76 the ratio of the heavy isotope to the light isotope (e.g., $^{18}O/^{16}O$; $^{17}O/^{16}O$) in the sample and

77 internationally recognized isotopic reference material (Vienna Standard Mean Ocean Water),

78 respectively. Several studies have suggested that the distinctive ($\Delta(^{17}O) = \delta(^{17}O) - 0.52 \times \delta(^{18}O)$)

79 and $\delta(^{18}O)$ signatures of atmospheric oxidants such as O_3, $O_2/RO_2/HO_2$, H_2O and OH are

80 incorporated into nitrate, tracking the oxidation chemistry of NO_x (Hastings et al., 2003; Michalski

81 et al., 2003; Savarino et al., 2007). Traditionally, the influence of O_3 incorporation in nitrate has

82 been quantitively tracked using only $\Delta(^{17}O)$, because of the unique mass-independent fractionation

83 that results in O_3 carrying excess $\delta(^{17}O)$, yielding a transferrable $\Delta(^{17}O) = (39\pm2)$ ‰ (Thiemens,

84 2006; Vicars and Savarino, 2014). However, all other atmospheric oxidants contain expected

85 mass-dependent signatures such that all have $\Delta(^{17}O)$ value of approximately 0 ‰. The $\delta(^{18}O)$ of

86 atmospheric oxidants could provide further insights into nitrate production mechanisms, especially

87 in cases where oxidants other than O_3 are important, since it is distinctive for each oxidant (e.g.,

88     $\delta(^{18}O, O_3) = (126.3\pm12)$ ‰, $\delta(^{18}O, O_2) = 23$ ‰, $\delta(^{18}O, OH) = -43$ ‰ (Michalski et al., 2012; Vicars

89   and Savarino, 2014)).

90

91   The northeastern US remains an important region to monitor due to historically degraded air

92   quality by NO_x emissions and negative atmospheric nitrate deposition impacts on sensitive

93   ecosystems. Changes in oxidation chemistry and chemical feedbacks associated with nitrate

94   production and deposition have important implications for predicting air quality improvements

95   and informing policy recommendations. In this study, using the Clean Air Status and Trends

96   Network (CASTNET) samples, we explored spatiotemporal differences in HNO_3 and pNO_3

97   concentrations and production mechanisms in the northeastern US over two years. Based on these

98   observations, we aimed to better constrain the mismatch in modeled predictions of atmospheric

99   nitrate chemistry in the northeastern US. This is the first study to quantitatively evaluate the triple

100   oxygen isotope composition from observations and model simulations in the northeastern US. The

101   comparison with the combination of $\Delta(^{17}O)$ and $\delta(^{18}O)$ values, and both gaseous and particle

102   phases of nitrate, provide a significant advance in our ability to probe the representation of

103   oxidation chemistry in atmospheric chemistry models.

104

105

2. Methods

2.1 CASTNET Samples

108   Atmospheric nitrate samples were collected by the US EPA at several locations of Clean Air Status

109   and Trends Network (CASTNET) sites in the northeastern US (**Figure 1**). Three CASTNET sites

110   were selected: Abington, CT (ABT147, 41.84° N, -72.01° W), Connecticut Hill, NY (CTH110,

111   42.40° N, -76.65° W), Woodstock, NH (WST109, 43.94° N, -71.70° W). The samples were

112   collected weekly from December 23, 2016, to December 28, 2018, using a three-stage filter pack

113   system. Based on EPA protocols, pNO_3 was collected using a Teflon filter in the first stage of the

114   filter pack, and gaseous HNO_3 was collected using a Nylon filter in the second stage of the filter

115   pack. We note that due to the semi-volatile characteristic of ammonium nitrate, some pNO_3 might

116   volatilize as HNO_3 and collect downstream of the filter pack leading to negative biases for pNO_3

117   and positive biases for HNO_3 collection (Hering and Cass, 1999; Ashbaugh and Eldred, 2004).

118

2.2 Concentration and Isotope Analyses

Filters were extracted and measured for nitrate concentration using Ion Chromatography and then stored in the CASTNET laboratory at room temperature for up to two years. Extracted samples were shipped to Brown University in the summer of 2020. Nitrate concentrations were measured at Brown University to check for stability of nitrate using standard colorimetric methods (i.e., US EPA Method 353.2) on an automated discrete UV-Vis Analyzer (SmartChem Westco Scientific Instruments, Inc.). The limit of detection was 0.1 and 0.3 µM for nitrite and nitrate, respectively, and the pooled standard deviation of replicate quality control standards was better than 3 %. Overall, strong positive correlations were found between measured concentrations at Brown and reported CASTNET data for both HNO_3 ($y = 0.99x - 0.08$ ($R^2 = 0.99$); $p < 0.05$) and pNO_3 ($y = 1.04x + 0.09$ ($R^2 = 0.99$); $p < 0.05$) (**Figure 2**); we, therefore, consider the samples representative of their original concentrations.

The samples were collected once a week, and equal volumes of filter extract were combined for isotope analysis to produce monthly aggregates for HNO_3 and pNO_3, respectively. Oxygen ($\delta(^{18}O)$ and $\Delta(^{17}O)$) stable isotopic compositions in HNO_3 and pNO_3 were analyzed utilizing the bacterial denitrifier method at Brown University (Sigman et al., 2001; Casciotti et al., 2002; Kaiser et al., 2007). Briefly, samples were injected into a buffer solution containing *P. aureofaciens,* which lack the nitrous oxide (N_2O) reductase enzyme, and sample nitrate was quantitatively reduced to N_2O. For $\delta(^{18}O)$ analysis, the generated N_2O is injected into a Thermo-Finnegan Delta V Plus isotope ratio mass spectrometry (IRMS) with a modified Gas Bench system after flowing through an automated extraction and purification system. Determination of $\delta(^{18}O)$ in N_2O was conducted at an *m/z* of 44, 45, and 46 and corrected using internationally recognized isotopic reference materials that included IAEA-NO_3 (25.6 ‰), USGS34 (-27.9 ‰), and USGS35 (57.5 ‰). The $\Delta(^{17}O)$ was determined in a separate analysis. The bacteria-generated N_2O was decomposed to N_2 and O_2 in a gold furnace heated to 770 ºC and analyzed at *m/z* 32, 33, and 34 to determine $^{17}O/^{16}O$ and $^{18}O/^{16}O$ ratios of the evolved O_2. The 33/32 and 34/32 mass ratios were corrected using isotopic reference materials, USGS34 (-0.29 ‰) and USGS35 (21.6 ‰), and then $\Delta(^{17}O)$ was determined from $\Delta(^{17}O) = \delta(^{17}O) - 0.52 \times \delta(^{18}O)$. Due to sample mass limitations, some samples were only analyzed for $\delta(^{18}O)$. The number of samples that were not measured for $\Delta(^{17}O)$ was 1 HNO_3 sample from CTH110, 2 HNO_3 samples from ABT147, 5 pNO_3 samples from CTH110, and 16 pNO_3 samples

150   from WST109. The overall pooled standard deviations of isotopic reference materials and sample

151   numbers were as followed: USGS34 ($\sigma(\delta(^{18}O))$ = 0.5 ‰ (n = 21); $\sigma(\Delta(^{17}O))$ = 1 ‰ (n = 26));

152   USGS35 ($\sigma(\delta(^{18}O))$ = 0.4 ‰ (n = 27); $\sigma(\Delta(^{17}O))$ = 2 ‰ (n = 26)), and IAEA-N3 ($\sigma(\delta(^{18}O))$ = 0.3

153   ‰ (n = 23)).

154

155   **2.3 GEOS-Chem Modeling**

156   The GEOS-Chem global model of atmospheric chemistry (Bey et al., 2001; Walker et al., 2012;

157   2019) was utilized to track the production of NO_2 and HNO_3 at the CASTNET sites and further to

158   model the oxygen isotope deltas (e.g., $\delta(^{18}O)$ and $\Delta(^{17}O)$) following a previous framework

159   (Alexander et al., 2020). Following this framework, oxidation chemistry is tagged only for HNO_3

160   production and is assumed to be the same for pNO_3. We use version 13.2.1

161   (doi:10.5281/zenodo.5500717) of the model driven by GEOS5-FP assimilated meteorology from

162   the NASA Global Modeling and Assimilation Office (GMAO). A nested grid (0.25° latitude ×

163   0.3125° longitude horizontal resolution; ~25 km) simulation was conducted over the northeastern

164   United States (97°-60° W; 35°-60º N) in 2017 and 2018. Boundary conditions were from global

165   simulations performed at 4° latitude × 5° longitude horizontal resolution for the same years after

166   a one-year initialization. Gas- and aerosol-phase chemistry was simulated using the default

167   "fullchem" mechanism (Bates and Jacob, 2019; Wang et al., 2021). Inorganic gas and aerosol

168   partitioning were conducted using version 2.2 of the ISORROPIA II thermodynamic equilibrium

169   model (Fountoukis and Nenes, 2007).

170

171   All default anthropogenic emissions were applied, which is primarily version 2.0 of the

172   Community Emissions Data System (Hoesly et al., 2018) as implemented by McDuffie et al.

173   (2020). Natural emissions respond to local meteorology and include biogenic VOCs from

174   terrestrial plants and the ocean (Millet et al., 2010; Guenther et al., 2012; Hu et al., 2015; Breider

175   et al., 2017), NO_x from lightning and soil microbial activity (Murray et al., 2012; Hudman et al.,

176   2012), mineral dust (Ridley et al., 2012), and sea salt (Jaeglé et al., 2011; Huang and Jaeglé, 2017).

177   Biomass burning emissions were monthly means from version 4.1s of the Global Fire Emissions

178   Database (GFED4.1s; van der Werf et al., 2017). Wet deposition for water-soluble aerosols is

179   described by Liu et al. (2001) and by Amos et al. (2012) for gases. Dry deposition is based on the

180   resistance-in-series scheme of Wesely (1989). Diagnostics were implemented to archive the total

181   production and loss pathways of NO_y, NO_x, NO_2, $RONO_2$, HNO_3 and pNO_3, including the net flux

182   of mass between HNO_3 and pNO_3 in ISOROPPIA II. We evaluated model performance for

183   simulating concentrations and isotope deltas ($\delta(^{18}O)$ and $\Delta(^{17}O)$) using the Normalized Mean Bias

184   (*B*) metric (Eq.1):

185    $B = (\sum (\bar{Q}_m - \bar{Q}_o) / \sum \bar{Q}_o)$ (Eq.1)

186   where $\bar{Q}_m$ = modeled quantities and $\bar{Q}_o$ = observed quantities.

187

188   **2.4 $\delta(^{18}O)$ and $\Delta(^{17}O)$ Calculations Based on Model Outputs**

189   The oxygen isotope deltas ($\delta(^{18}O)$ and $\Delta(^{17}O)$) of nitrate were calculated based on oxygen isotope

190   mass-balance using production rate outputs from the GEOS-Chem global 3-D model and

191   compared with our observations. Expected $\delta(^{18}O)$ and $\Delta(^{17}O)$ ranges resulting from nitrate

192   production pathways have been previously described and calculated using oxygen mass-balance

193   (Alexander et al., 2009, 2020; Michalski et al., 2003; Morin et al., 2011; Carter et al., 2021). Briefly,

194   the $\delta(^{18}O)$ and $\Delta(^{17}O)$ of nitrate are determined by both NO_x photochemical cycling and nitrate

195   formation reactions (Alexander et al., 2009; Walters et al., 2018). During NO_x photochemical

196   cycling, the oxygen isotopic compositions of NO_x are determined by the relative production rates

197   of NO_2 via reaction of NO with O_3, peroxy and hydroperoxyl radicals, and halogen oxides (XO;

198   BrO, ClO). The proportional contribution of O_3 during NO oxidation is denoted as *A* and is

199   calculated using

200

201    $A = (k(O_3+NO)\,[O_3] + k(XO+NO)[XO])/(k(O_3+NO)[O_3] + k(XO+NO)[XO] + k(HO_2+NO)[HO_2]$

202    $+ k(RO_2+NO)[RO_2])$ (Eq. 2)

203

204   where k is the respective rate constant for NO oxidation via O_3, XO, HO_2, and RO_2. The $\Delta(^{17}O)$

205   value of the terminal oxygen atom in O_3 (O_3^*) is assumed to be (39±2) ‰ based on observations,

206   while all other oxidants are assumed to be 0 ‰ (Vicars et al., 2012; Vicars and Savarino, 2014;

207   Alexander et al., 2020). $\delta(^{18}O)$ and $\Delta(^{17}O)$ values of nitrate from each production pathway were

208   then determined using O mass-balance based on the O transfer from varying oxidants involved in

209   its formation (**Table 1**).

210

211 The GEOS-Chem global model has been previously used to quantify nitrate production pathways
212 based on $\Delta(^{17}O)$ (Alexander et al., 2009, 2020), but this has not been done for $\delta(^{18}O)$. Using a
213 similar framework as for $\Delta(^{17}O)$, we expect that $\delta(^{18}O)$ of NO_2 reflects isotopic signatures of both
214 O_3 and O_2, as it has been assumed that the O isotopic composition of RO_2 and HO_2 is equal to O_2
215 (Michalski et al, 2012; Walters et al., 2018). Accordingly, the values of $\delta(^{18}O, NO_2)$ can be
216 predicted by the proportional contribution of O_3 and both HO_2 and RO_2 during NO_x cycling with
217 their distinct $\delta(^{18}O)$ values of O_3 and O_2 (Eq. 3; **Table 1**).
218
219 $\delta(^{18}O, NO_2) = A(\delta(^{18}O, O_3^*)) + (1-A)(\delta(^{18}O, O_2))$ (Eq.3)
220
221 The $\delta(^{18}O)$ values of O_3 and O_2 are adopted from previous studies that determined $\delta(^{18}O, O_3^*)$ and
222 $\delta(^{18}O, O_2)$ as 126.3 ‰ and 23 ‰ (Vicars and Savarino, 2014; Kroopnick and Craig, 1972,
223 respectively). For the calculation of $\delta(^{18}O)$ of nitrate, the value of $\delta(^{18}O)$ of $H_2O(l)$ is assumed to
224 be -6 ‰, which is a typical mid-latitude value and represents water in the liquid phase incorporated
225 into nitrate formation associated with heterogeneous reactions by N_2O_5 or NO_2 hydrolysis
226 (Michalski et al, 2012). The $\delta(^{18}O)$ value of OH can be dependent on both O_3 and $H_2O(g)$, as well
227 as environmental conditions since oxygen in OH can exchange with $H_2O(g)$ (Dubey et al. 1997).
228 Fractionation factors associated with the O transfer into NO_y products are unknown and therefore
229 were not considered. The $\delta(^{18}O)$ of $H_2O(g)$ was estimated based on the equilibrium between $H_2O(l)$
230 and $H_2O(g)$ with a temperature-dependent fractionation factor (1.0094 at 298K); it is assumed that
231 OH and $H_2O(g)$ exist in isotopic equilibrium, which has a theoretically determined fractionation
232 factor (1.0371 at 298K) and leads to an estimate of $\delta(^{18}O, OH)$ of -43 ‰ (Michalski et al, 2012;
233 Walters and Michalski, 2016). We note that the typical annual temperature for the northeast US is
234 approximately 287 K, yielding a $\delta(^{18}O, OH)$ of -45 ‰; for comparison purposes with prior
235 publications, we utilize -43 ‰, which makes little difference in the quantitative results below. In
236 the final step, $\delta(^{18}O)$ or $\Delta(^{17}O)$ of total atmospheric nitrate were calculated based on the monthly-
237 averaged production rates from GEOS-Chem and the seven major reactions that produce nitrate in
238 the model (**Table 1**) to compare with observations.
239
240
241 **3. Results and Discussion**

3.1 Spatiotemporal Variations of Atmospheric Nitrate Concentration

Figure 3 shows the monthly averaged spatiotemporal variations of HNO_3 and pNO_3 mass concentration (denoted as γ). The observed (o) HNO_3 concentrations ($\gamma_o(HNO_3)$) ranged from 0.11 $\mu g\ m^{-3}$ to 0.88 $\mu g\ m^{-3}$, with a mean value of 0.46 $\mu g\ m^{-3}$ across the three CASTNET sites. The observed pNO_3 concentrations ($\gamma_o(pNO_3)$) ranged from 0.04 $\mu g\ m^{-3}$ to 2.01 $\mu g\ m^{-3}$, with a mean value of 0.50 $\mu g\ m^{-3}$, and showed clear seasonality at all three sites with averaged higher values (0.75 ± 0.52) $\mu g\ m^{-3}$ in the cold season (October to March) and lower values (0.25 ± 0.17) $\mu g\ m^{-3}$ in the warm season (April to September), which were significantly different ($p < 0.01$). On the other hand, $\gamma_o(HNO_3)$ was seasonally invariable with (0.42 ± 0.17) $\mu g\ m^{-3}$ for cold season and (0.50 ± 0.24) $\mu g\ m^{-3}$ for warm season that was not statistically different ($p > 0.05$). Averaged $\gamma_o(HNO_3)$ was generally lower than pNO_3 across the sites, but the difference was statistically insignificant ($p > 0.05$). Both $\gamma_o(HNO_3)$ and $\gamma_o(pNO_3)$ indicated spatial variability with higher values at ABT147 and CTH110 than the WST109 site. The mean annual $\gamma_o(HNO_3)$ and $\gamma_o(pNO_3)$ were (0.61 ± 0.15) $\mu g\ m^{-3}$ and (0.66 ± 0.34) $\mu g\ m^{-3}$ at ABT147, (0.55 ± 0.13) $\mu g\ m^{-3}$ and (0.68 ± 0.58) $\mu g\ m^{-3}$ at CTH110, and (0.22 ± 0.06) $\mu g\ m^{-3}$ and (0.17 ± 0.13) $\mu g\ m^{-3}$ at WST109, respectively.

The modeled (m) HNO_3 concentrations ($\gamma_m(HNO_3)$) ranged from 0.20 $\mu g\ m^{-3}$ to 2.36 $\mu g\ m^{-3}$, with a mean value of 0.82 $\mu g\ m^{-3}$ and modeled pNO_3 concentrations ($\gamma_m(pNO_3)$) ranged from 0.20 $\mu g\ m^{-3}$ to 5.27 $\mu g\ m^{-3}$, with a mean value of 1.89 $\mu g\ m^{-3}$. Contrary to our observed data, no consistent spatial variability was observed for $\gamma_m(HNO_3)$ and $\gamma_m(pNO_3)$. The mean $\gamma_m(HNO_3)$ and $\gamma_m(pNO_3)$ were (1.09 ± 0.62) $\mu g\ m^{-3}$ and (1.73 ± 1.13) $\mu g\ m^{-3}$ at ABT147, (0.74 ± 0.46) $\mu g\ m^{-3}$ and (2.42 ± 1.71) $\mu g\ m^{-3}$ at CTH110, and (0.64 ± 0.22) $\mu g\ m^{-3}$ and (1.52 ± 1.24) $\mu g\ m^{-3}$ at WST109, respectively. However, there are significant seasonal model biases for the HNO_3 and pNO_3. The model significantly overestimates pNO_3 during the winter (3-9 times) and overestimates HNO_3 during the summer (2-3 times).

As stated above, there can be negative biases for pNO_3 and positive biases for HNO_3 collection, but these should be reduced by comparing the model to total atmospheric nitrate ($tNO_3 = HNO_3 + pNO_3$). Still, the simulated tNO_3 concentration ($\gamma_m(tNO_3)$) with GEOS-Chem is notably

272 overestimated relative to observations (γ_o(tNO$_3$); $B = 182$ %; **Figure 3**). While the simulated pNO$_3$

273 well reproduce the observed seasonality (high concentrations in the cold season and vice versa), it

274 highly overestimated the concentrations for most of the year ($B = 276$ %; **Figure 3**). The simulated

275 HNO$_3$ did not capture the observed relative lack of seasonality, instead showing clear seasonality

276 with generally high concentrations in the warm season and low in the cold season. The lack of

277 agreement between GEOS-Chem and nitrate observations is consistent with previously reported

278 results in other studies (Heald et al., 2012; Zhang et al., 2012; Walker et al., 2012). Uncertainties

279 in N$_2$O$_5$ hydrolysis rate, emission estimates, or dry and wet deposition removal rates have been

280 suggested as possible causes for predicted nitrate biases. For instance, Luo et al., 2019; 2020

281 reported dramatic improvement of nitric acid and nitrate biases by updating wet scavenging

282 parameterization in the GEOS-Chem model; however, this update leads to biases in oxidized

283 nitrogen wet deposition between model predictions and observations.

284

285 **3.2 Oxygen Isotopic Compositions – Oxidation Chemistry and Phase Difference**

286

287 The oxygen isotopic compositions in atmospheric nitrate are used to evaluate NO$_x$ oxidation

288 chemistry and to assess seasonal changes in nitrate formation mechanisms. For the CASTNET

289 sites, the Δ(^{17}O, HNO$_3$) and Δ(^{17}O, pNO$_3$) values ranged from 12.9 ‰ to 30.9 ‰ and from 16.6 ‰

290 to 33.7 ‰, with a mean value of (22.7±3.6) ‰ and (27.1±3.8) ‰, respectively **(Figure 4)**. The

291 δ(^{18}O, HNO$_3$) and δ(^{18}O, pNO$_3$) values ranged from 46.9 ‰ to 82.1 ‰ and from 43.6 ‰ to 85.3

292 ‰, with a mean value of (68.1±7.1) ‰ and (68.2±8.3) ‰, respectively **(Figure 5)**. These

293 observations are in the range of previously reported values in polluted mid-latitudes: δ(^{18}O, HNO$_3$)

294 and δ(^{18}O, pNO$_3$) in CASTNET sites in Ohio, Pennsylvania, and New York from April 2004 to

295 March 2005 ranged from 51.6 ‰ to 94.0 ‰ and from 45.2 ‰ to 92.7 ‰ (Elliott et al., 2009),

296 respectively. They are also consistent with observations of polluted air masses in Canada from

297 September 2010 to January 2014, which were from 62.4 to 81.7 ‰ for δ(^{18}O, HNO$_3$), from 19.3

298 to 29.0 ‰ for Δ(^{17}O, HNO$_3$), from 48.4 to 83.2 ‰for δ(^{18}O, pNO$_3$), and from 13.8 to 30.5 ‰ for

299 Δ(^{17}O, pNO$_3$) (Savard et al., 2018).

300

301 Previous studies and modeling results have indicated that the seasonality of oxygen isotopic

302 compositions in HNO$_3$ and pNO$_3$ is driven by a shift in oxidation chemistry (e.g., Hastings et al.,

303   2003; Michalski et al, 2012; Alexander et al., 2009; 2020). Globally, the seasonality reflects a shift

304   in O_3 to HO_x radical chemistry during winter to summer, respectively. Wintertime has higher NO

305   + O_3 branching ratios than summer, which has increased NO + RO_2/HO_2. The high values of $\delta(^{18}O)$

306   and $\Delta(^{17}O)$ in HNO_3 and pNO_3 during the cold season are caused by the increased incorporation

307   of O_3 into the nitrate product through N_2O_5 heterogeneous hydrolysis on aerosols (**Figures 4 and**

308   **5**). In contrast, the dominance of gas-phase production by the NO_2 + OH reaction dilutes the

309   isotopic influence of O_3 during warm seasons leading to the low values of $\delta(^{18}O)$ and $\Delta(^{17}O)$ in

310   HNO_3 and pNO_3. Spatial variability is observed in $\delta(^{18}O)$ and $\Delta(^{17}O)$ of HNO_3, with highest values

311   at CTH110 ($\delta(^{18}O)$: (71.5±5.6) ‰ (n = 24) and $\Delta(^{17}O)$: (25.0±3.1) ‰ (n = 23)) followed by

312   ABT147 ($\delta(^{18}O)$: (70.1±4.8) ‰ (n = 24) and $\Delta(^{17}O)$: (23.1±2.2) ‰ (n = 24)) and WST109 ($\delta(^{18}O)$:

313   (62.8±7.7) ‰ (n = 24) and $\Delta(^{17}O)$: (20.2±3.7) ‰ (n = 24)). However, $\delta(^{18}O)$ and $\Delta(^{17}O)$ of pNO_3

314   were not significantly different across the stations: for ABT147 ($\delta(^{18}O)$: (68.6±7.1) ‰ (n = 24)

315   and $\Delta(^{17}O)$: (26.4±3.6) ‰ (n = 22)); CTH110 ($\delta(^{18}O)$: (69.1±8.9) ‰ (n = 24) and $\Delta(^{17}O)$: (26.8±4.1)

316   ‰ (n = 19)); and WST109 ($\delta(^{18}O)$: (66.8±8.7) ‰ (n = 24) and $\Delta(^{17}O)$: (29.4±2.9) ‰ (n = 10)).

317

318   Our observations indicate a significant phase-dependent difference in oxidation chemistry between

319   HNO_3 and pNO_3 that is unexpected (**Figure 6**). Many modeled mechanisms of gas- and aqueous-

320   phase chemistry produce HNO_3, then HNO_3 is partitioned into the aerosol phase based on

321   thermodynamic equilibrium (i.e., $NH_4NO_3(s) \rightleftharpoons HNO_3(g) + NH_3(g)$) or coarse uptake.

322   Conventional understanding would expect $\Delta(^{17}O)$ of HNO_3 and pNO_3 to be the same (e.g.,

323   Alexander., 2020). However, observed $\Delta(^{17}O, pNO_3)$ tends to be significantly higher than $\Delta(^{17}O,$

324    $HNO_3)$ ($p < 0.01$ at ABT and CTH, $p = 0.088$ at WST). The difference between $\Delta(^{17}O, pNO_3)$ and

325    $\Delta(^{17}O, HNO_3)$ was larger in the cold season than in the warm season. For example, on average,

326    $\Delta(^{17}O, pNO_3)$ was (5.1±2.6 ‰) higher than $\Delta(^{17}O, HNO_3)$ during the cold months, while $\Delta(^{17}O,$

327    $pNO_3)$ was (2.7±4.7 ‰) higher than $\Delta(^{17}O, HNO_3)$ during warm months. This phase difference in

328    $\Delta(^{17}O)$ cannot be explained by potential sample biases caused by volatilization, which leads to

329   mass-dependent fractionation. This difference might be related to the differences in particulate

330   nitrate size-dependent production pathways. Previous studies of size-segregated $\Delta(^{17}O, pNO_3)$

331   indicated higher values for coarse pNO_3 (aerodynamic diameter (D_a) > 0.95 μm) relative to fine

332   pNO_3 (D_a < 0.95 μm) that was concluded to reflect the increased importance of heterogeneous

333   N_2O_5 hydrolysis on coarse particles relative to fine particles (Vicars et al., 2013). The CASTNET

334   pNO$_3$ samples reflect total suspended particles (TSP) such that increased importance of N$_2$O$_5$

335   heterogeneous chemistry for coarse particulate nitrate formation could explain the higher Δ(^{17}O,

336   pNO$_3$) values we observe relative to Δ(^{17}O, HNO$_3$).

337

338   Positive linear relationships between δ(^{18}O) and Δ(^{17}O) were observed for HNO$_3$ and pNO$_3$ across

339   the CASTNET sites, with similar slopes but different oxygen isotopic signatures indicated by

340   different intercepts (**Figure 6**). For the relationship of δ(^{18}O) and Δ(^{17}O), the high end-member

341   should result from O$_3$, and the lower end-member depends on the isotopic signature of the

342   atmospheric oxidants involved. The transferable δ(^{18}O) signatures of atmospheric oxidants are not

343   fully understood yet, reflecting a complex combination of atmospheric oxidant source signatures

344   and isotope fractionation during reaction and incorporation into the nitrate end-product. While

345   ozone has a notably high Δ(^{17}O) value ((39±2) ‰; Vicars and Savarino, 2014), Δ(^{17}O) values of

346   other atmospheric oxidants such as O$_2$/RO$_2$/HO$_2$, H$_2$O and OH are equal to or close to 0 ‰

347   (Michalski et al., 2012; Walters et al., 2019). Overall, our results suggest more O$_3$ is incorporated

348   during the formation of pNO$_3$ than HNO$_3$. We further analyze the oxidation chemistry involved in

349   atmospheric nitrate formation based on output from the GEOS-Chem chemical transport model.

350

351   **3.3 Quantifying atmospheric nitrate oxidation chemistry using Δ(^{17}O)**

352   Observations of the oxygen isotopic composition were utilized to quantify the relative importance

353   of different nitrate formation pathways and to assess model representation of the chemistry of

354   nitrate formation. Using atmospheric nitrate production rates from the GEOS-Chem model ("base

355   case"), Δ(^{17}O) was calculated within a grid cell corresponding to our CASTNET sites and

356   compared with observed Δ(^{17}O, HNO$_3$, pNO$_3$) at each site **(Figure 4)**. We note that the previous

357   Δ(^{17}O) GEOS-Chem framework tags NO$_2$ and HNO$_3$ production and assumes that pNO$_3$

358   production is similar to HNO$_3$ due to thermodynamic equilibrium. Thus, we compared the

359   simulated Δ(^{17}O, HNO$_3$) from GEOS-Chem to our Δ(^{17}O, HNO$_3$) and Δ(^{17}O, pNO$_3$) observations.

360   The averaged residuals over the collection period for each site were 3.9 ‰, 2.8 ‰, and 5.6 ‰ for

361   Δ(^{17}O, HNO$_3$), and 1.5 ‰, 1.7 ‰, and 6.1 ‰ for Δ(^{17}O, pNO$_3$) at ABT147, CTH110, and WST109,

362   respectively **(Figure 4)**. Calculated Δ(^{17}O) based on GEOS-Chem output reproduced the observed

363   temporal variations well **(Figure 4)**, although the model better captured the lower observed Δ(^{17}O)

364   during warmer months versus the higher values observed in the cooler months (**Table 2**). The

365   GEOS-Chem model also does not capture observed spatial $\Delta(^{17}O)$ variabilities. For instance,

366   higher $\Delta(^{17}O)$ values (especially for HNO_3) were observed at CTH110 compared to WST109;

367   while no significant spatial $\Delta(^{17}O)$ differences were predicted from GEOS-Chem. The model

368   prediction was sensitive to the type of nitrate; the calculated $\Delta(^{17}O)$ showed a better agreement

369   with observed $\Delta(^{17}O)$ of pNO_3 ($y = 0.55\ x + 12.62$ ($R^2 = 0.48$)) than $\Delta(^{17}O)$ of HNO_3 ($y = 0.46\ x +$

370   10.68 ($R^2 = 0.44$)) at all CASTNET sites ($B = $ -2 % and 15 %, respectively) (**Figure 7**).

371

372   Several studies have used $\Delta(^{17}O)$ to quantify and/or constrain modeled chemical mechanisms. Here,

373   GEOS-Chem nitrate production rates and thus calculated $\Delta(^{17}O)$ were optimized to find the lowest

374   residual sum of squares between the calculated and observed $\Delta(^{17}O)$. This optimization algorithm

375   constrains the relative rates of nitrate formation pathways simulated by GEOS-Chem.

376   Additionally, the optimization was conducted for HNO_3 and pNO_3 separately. Calculated $\Delta(^{17}O)$

377   from the base GEOS-Chem model was generally 1.15 times higher than observed $\Delta(^{17}O, HNO_3)$

378   and 0.98 times lower than $\Delta(^{17}O, pNO_3)$ across all CASTNET sites. After optimization, the

379   residuals between observed and calculated $\Delta(^{17}O)$ dramatically decreased (**Figure 4),** especially in

380   the cold season **(Table 2)**. Moreover, the linear relationships had slopes much closer to the 1:1 line

381   (i.e., from 0.46 to 1.03 for HNO_3 and from 0.55 to 0.78 for pNO_3**; Figure 7**) than the base GEOS-

382   Chem model across the three CASTNET site (the relationships for each site before and after

383   optimization are shown in **Figure 7**). On a subannnual basis, the $\Delta(^{17}O)$ comparison for the cold

384   season showed better improvement than the warm season, especially for $\Delta(^{17}O, HNO_3)$.

385

386   The dominant annual pathway for nitrate formation in the GEOS-Chem model ("base case") was

387   N_2O_5 hydrolysis, which accounts for 50 % **(Figure 8)**, followed by $NO_2 + OH$ (31 %) and $RONO_2$

388   hydrolysis (13 %) across all CASTNET sites. Nitrate production via the reaction of XNO_3

389   hydrolysis and $NO_3 + HC$ was small (< 1 %) at all sites. Strong seasonality in nitrate production

390   was observed, as expected, with high portions of N_2O_5 hydrolysis in winter and $NO_2 + OH$ in

391   summer **(Figure 8)**.

392

393   After optimization, the dominant pathway for nitrate formation in GEOS-Chem changed compared

394   to the base case. For $\Delta(^{17}O, pNO_3)$, $NO_2 + OH$ (60 %) was the dominant pathway for nitrate

395   formation in the optimized GEOS-Chem calculation, followed by N_2O_5 hydrolysis (31 %) and

396 NO$_3$ hydrolysis (4 %) **(Figure 8)**. At the same time, $\Delta(^{17}O, HNO_3)$ was almost entirely driven by

397 NO$_2$ + OH reaction (98 %) in the optimized GEOS-Chem case **(Figure 8)**. The optimized GEOS-

398 Chem calculations suggest that the fraction of nitrate produced by N$_2$O$_5$ hydrolysis was

399 significantly overestimated in the GEOS-Chem base case. In the base case, N$_2$O$_5$ hydrolysis

400 dominated nitrate production, especially in the cold season with a fraction of over 68 % at all

401 CASTNET sites **(Figure 8)**. This may also partly explain major nitrate concentration overestimates,

402 particularly in the cold season.

403

404 **3.4 Modeling $\delta(^{18}O)$ of Atmospheric Nitrate**

405 The GEOS-Chem model $\delta(^{18}O)$ was also calculated in the same manner as $\Delta(^{17}O)$ **(Figure 5)**.

406 Unlike the calculated $\Delta(^{17}O)$, calculated $\delta(^{18}O)$ showed remarkably positive biases compared with

407 measured $\delta(^{18}O)$ of HNO$_3$ ($B = 22$ %) and pNO$_3$ ($B = 21$ %). The averaged residuals for $\delta(^{18}O,$

408 HNO$_3$) at each site were 13.9 ‰, 12.9 ‰, and 19.6 ‰, and for $\delta(^{18}O, pNO_3)$ were 15.4 ‰, 14.2

409 ‰, and 18.2 ‰ at ABT147, CTH110, and WST109, respectively **(Figure 5, Table 2)**. Modeling

410 the $\delta(^{18}O)$ values of nitrate is more challenging than $\Delta(^{17}O)$ because not all oxidant $\delta(^{18}O)$ values

411 have been directly observed and fractionation factors associated with the O transfer into NO$_y$

412 products are unknown. Uncertainty in $\delta(^{18}O)$ values could be a major factor causing disagreement

413 between observed and calculated $\delta(^{18}O)$. Additionally, uncertainties in the gas-phase and aerosol

414 scheme related to tNO$_3$ production in GEOS-Chem could account for the discrepancy. Still, as

415 with $\Delta(^{17}O)$, the calculated $\delta(^{18}O)$ showed far more disagreement with observations during cooler

416 months than warmer months **(Table 2)**.

417

418 Newly optimized nitrate production in GEOS-Chem was also applied to $\delta(^{18}O)$ calculation and

419 compared with previous results. As with $\Delta(^{17}O)$, a slope of the regression line between (optimized)

420 calculated and observed $\delta(^{18}O)$ became closer to 1 (i.e., from 0.30 to 0.74 for HNO$_3$ and from 0.39

421 to 0.49 for pNO$_3$; **Figure 9**) and residuals improved at each site after the optimization **(Figure 5)**.

422 Overall, the optimized GEOS-Chem $\delta(^{18}O)$ calculation showed better agreement than the base

423 GEOS-Chem model ($B = -6$ % for $\delta(^{18}O, HNO_3)$ and $B = 13$ % for $\delta(^{18}O, pNO_3)$). The most

424 significant improvement, as shown by the residuals, is during the cold season.

425

426 **3.5 $\delta(^{18}O)$ Optimization of Atmospheric Oxidants**

427 After optimization of relative nitrate production rates in GEOS-Chem based on $\Delta(^{17}O)$, we applied
428 the optimized chemical production to calculate $\delta(^{18}O)$, but still observed discrepancy between
429 observed and predicted $\delta(^{18}O)$. The discrepancy could be related to variable and somewhat
430 unconstrained $\delta(^{18}O)$ values of atmospheric oxidants important for nitrate formation. To test this,
431 the assumed (literature) $\delta(^{18}O)$ values of oxidants were optimized by selecting the best linear fit
432 between the observations and calculated $\delta(^{18}O$, HNO_3 and pNO_3) **(Figure 10)**. After optimization
433 for $\delta(^{18}O)$ of oxidants, the discrepancy between observation and calculation was dramatically
434 reduced **(Figure 9)** with a decrease in B from 21 to 1 %. The optimization predicted $\delta(^{18}O)$ of H_2O
435 values similar to what was expected (-6.5 ‰ vs. -6.0 ‰), however different values were predicted
436 for $\delta(^{18}O)$ of O_2, OH, and O_3 (**Table 3**). A typical mid-latitude value (-6 ‰) of $\delta(^{18}O$, $H_2O)$ was
437 selected in this study. We note that the $\delta(^{18}O$, $H_2O)$ will vary seasonally; however, the calculated
438 $\delta(^{18}O)$ value of nitrate was insensitive to this value because of the relatively minor role that H_2O
439 contributes to O atoms of atmospheric nitrate. For $\delta(^{18}O)$ of O_2, OH, and O_3, it is possible that this
440 reflects isotope effects associated with the incorporation of these oxidants during nitrate
441 production, rather than further issues with model chemistry since the relative production rates here
442 are constrained based on $\Delta(^{17}O)$. The $\delta(^{18}O$, $O_2)$ was the best fit with calculated $\delta(^{18}O)$ of nitrate
443 values when assuming a value of 11.1 ‰ (vs. the well-known 23 ‰). Since atmospheric O_2 is
444 incorporated into nitrate via NO oxidation by HO_2 and RO_2 radicals, it was assumed that the $\delta(^{18}O)$
445 value of RO_2 and HO_2 is equal to O_2 such that this does not consider any potential isotope effects
446 associated with HO_2 and RO_2 formation and reaction with NO. The optimized value of 11 ‰
447 reflects the O atom derived from RO_2/HO_2 reactions incorporated into NO_2. Thus, our optimized
448 value might suggest that RO_2/HO_2 singly substituted with ^{18}O (e.g., $R^{18}O^{16}O$, $H^{18}O^{16}O$) reacts
449 slower than the ^{16}O isotopologues (e.g., $R^{16}O_2$ or $H^{16}O_2$).

450

451 The observed $\delta(^{18}O)$ of O_3 and OH for the CASTNET samples were the best fit with calculated
452 $\delta(^{18}O)$ when assuming values of 89.9 ‰ for $\delta(^{18}O$, $O_3)$ and 42.2 ‰ for $\delta(^{18}O$, OH), respectively.
453 In the previous section, we noted that NO_2 + OH and N_2O_5 hydrolysis reactions were the dominant
454 pathways for nitrate formation, indicating that OH and O_3 play an important role in determining
455 the $\delta(^{18}O)$ value in nitrate. Indeed, optimizing $\delta(^{18}O)$ values to find the best agreement between
456 observation and calculation is largely dependent on $\delta(^{18}O)$ values of O_3 and OH (see also **Table**
457 **3**). The optimized $\delta(^{18}O$, $O_3{}^*)$ value (89.9 ‰) was lower than the average reported $\delta(^{18}O$, $O_3{}^*)$

458 ((~126±12) ‰; Vicars and Savarino, 2014), though the $\delta(^{18}O, O_3)$ is known to vary with
459 temperature and pressure, and could also potentially be fractionated during reactions
460 (Brenninkmeijer et al., 2004). For example, Walters and Michalski (2016) calculated an isotopic
461 enrichment factor near -20 ‰ associated with O_3 transfer in its reaction with NO, which would
462 lower the transferable $\delta(^{18}O)$ of O_3, consistent with our predictions. The isotope effect for NO +
463 O_3 reaction is the only one currently known; in other words, no other $\delta(^{18}O)$ isotope effects
464 associated with O_3 reaction with NO_y (e.g., $NO_2 + O_3$) have been calculated. Further, there is
465 potential for equilibrium isotope effects between N_2O_5, NO_2, and NO_3 that could also impart a
466 mass-dependent $\delta(^{18}O)$ fractionation. While difficult to pinpoint the exact isotope effects occurring,
467 our optimized value predicts an elevated $\delta(^{18}O)$ value derived from O_3 compared to the other
468 oxidants, consistent with our expectation.

469

470 For $\delta(^{18}O, OH)$, the optimized value dramatically increased compared to the initial assumed value
471 (-43.0 ‰). The initial $\delta(^{18}O, OH)$ value is based on several assumptions that may not be correct
472 regarding isotope exchange with $H_2O(g)$. Additionally, Fang et al. (2021) suggested that $\delta(^{15}N)$ of
473 nitrate is largely controlled by an isotope effect in the $NO_2 + OH$ pathway, and it could be
474 conceivable that $\delta(^{18}O)$ may be affected by a similar isotope effect as well. Overall, the
475 optimization of $\delta(^{18}O, OH)$ is highly dependent on the $\delta(^{18}O, O_3^*)$ (see **Table 3**), which makes
476 sense given the proportional control of the $NO_2 + OH$ and N_2O_5 hydrolysis reactions. Despite the
477 uncertainty in the transferrable $\delta(^{18}O)$ from major oxidants, the comparison between predicted and
478 observed $\delta(^{18}O)$ and $\Delta(^{17}O)$ both suggest a larger relative importance of $NO_2 + OH$ chemistry than
479 reflected in the model simulations. We note here that this finding is consistent with our companion
480 study (acp-2022-621) of $\delta(^{15}N, HNO_3)$ and $\delta(^{15}N, pNO_3)$ as well.

481

482 Overall, the observed differences in the oxygen isotopic composition of HNO_3 and pNO_3, the
483 observed relationships of $\delta(^{18}O)$ and $\Delta(^{17}O)$ in the different nitrate phases, and the significant
484 mismatch with the global model base case challenge our current representation of nitrate chemistry
485 in atmospheric chemistry models. Generally, the GEOS-Chem $\Delta(^{17}O)$ simulations were biased
486 high relative to observations, indicating the over-incorporation of O_3 during nitrate formation. The
487 largest discrepancies in the model-observation comparisons, particularly for pNO_3, occur in winter.
488 Our optimized chemistry, constrained by the observed $\delta(^{18}O)$ and $\Delta(^{17}O)$, suggested that the

489   heterogenous production of nitrate via N_2O_5 chemistry is currently significantly overestimated.
490   While our focus is on the northeastern US, an area of important environmental change due to
491   regulated emissions reductions, this finding has implications for the global modeling of
492   atmospheric nitrate and oxidation chemistry.

493

494   **4. Conclusions**

495

496   Using a combination of concentration and isotopic analyses, we evaluated atmospheric nitrate
497   formation pathways in the northeastern US in 2017–2018. The GEOS-Chem model showed large
498   positive biases for HNO_3 and pNO_3 concentrations, an important issue that is common in
499   atmospheric chemistry models. The observed oxygen isotopic compositions ($\Delta(^{17}O)$ and $\delta(^{18}O)$)
500   revealed a more important relative role of NO_2+OH chemistry and indicated that the model
501   chemistry overpredicted heterogeneous hydrolysis of N_2O_5 for atmospheric nitrate in the
502   northeastern US. We also observed nitrate-phase differences in $\Delta(^{17}O)$ and $\delta(^{18}O)$, which are not
503   captured in current models. Further investigation of size-segregated nitrate chemistry is
504   recommended to improve model prediction of nitrate formation.

505

506   Additionally, this finding has important implications for predicting oxidation chemistry in the
507   atmosphere. For instance, the production of nitrate via heterogeneous hydrolysis of N_2O_5
508   represents a radical termination process, such that a much-reduced importance of this reaction
509   could yield more radical chemistry with an impact on oxidant concentrations. Indeed, an important
510   mechanism for converting NO_x to atmospheric nitrate could affect controlling the oxidizing
511   efficiency, which directly influences the atmospheric oxidation budget and many atmospheric
512   pollutants' (notably greenhouse gases) lifetime in the atmosphere. Thus, better constraining their
513   chemistries and feedbacks is crucial to understanding atmospheric nitrate production pathways and
514   its connection to atmospheric oxidation chemistry.

515

516   Traditionally, $\Delta(^{17}O)$ has been used to quantitatively assess nitrate production pathways. The use
517   of $\delta(^{18}O)$ as well can enhance our understanding of the oxidants contributing to nitrate formation,
518   particularly for distinguishing oxidants that have similar $\Delta(^{17}O)$ values (i.e., all are near 0 ‰ except
519   ozone). However, our study also observed a discrepancy between observed and calculated $\delta(^{18}O)$

520 values, even after accounting for an optimized chemical production based on $\Delta(^{17}O)$. The best
521 match of the observations suggests that the transferrable $\delta(^{18}O)$ values of oxidants may vary more
522 than is currently suggested in the literature. Improved constraints, particularly on the isotopic
523 composition of OH and variability in $\delta(^{18}O, O_3)$ would add critical value to modeling and
524 interpretation of major oxidation chemistry in the atmosphere.

525

526 **Data Availability.** Data presented in this article are available on the Harvard Dataverse at
527 https://doi.org/10.7910/DVN/X6BB1I, US EPA CASTNET database.

528

529 **Author Contributions.** HK, WWW, MGH designed the varying aspects of the study. CB and
530 WWW carried out the laboratory measurements. HK interpreted data, conducted statistical
531 analysis, and analyzed model results. LTM contributed GEOS-Chem simulations. HK and WWW
532 prepared the article with contributions from all co-authors.

533

534 **Acknowledgements.** We thank Ruby Ho for sampling and laboratory assistance. We are grateful
535 to the US EPA CASTNET program and staff for their cooperation in this study and assistance with
536 receiving archived samples for isotopic analysis.

537

538 **Competing Interests.** The authors declare no competing financial interest.

539

540 **Financial Support.** National Science Foundation (AGS-2002750); Institute at Brown for
541 Environment and Society Seed Grant; Voss Environmental Fellowship from the Institute at Brown
542 for Environment and Society

543
544
545 **Reference**
546

547 Alexander, B., Hastings, M. G., Allman, D. J., Dachs, J., Thornton, J. A., and Kunasek, S. A.:
548   Quantifying atmospheric nitrate formation pathways based on a global model of the oxygen
549   isotopic composition ($\Delta^{17}O$) of atmospheric nitrate, Atmospheric Chemistry and Physics, 9,
550   5043–5056, 2009.
551 Alexander, B., Sherwen, T., Holmes, C. D., Fisher, J. A., Chen, Q., Evans, M. J., and Kasibhatla,
552   P.: Global inorganic nitrate production mechanisms: comparison of a global model with nitrate
553   isotope observations, Atmospheric Chemistry and Physics, 20, 3859–3877, 2020.

Amos, H. M., Jacob, D. J., Holmes, C. D., Fisher, J. A., Wang, Q., Yantosca, R. M., Corbitt, E. S., Galarneau, E., Rutter, A. P., and Gustin, M. S.: Gas-particle partitioning of atmospheric Hg (II) and its effect on global mercury deposition, Atmospheric Chemistry and Physics, 12, 591–603, 2012.

Ashbaugh, L. L. and Eldred, R. A.: Loss of Particle Nitrate from Teflon Sampling Filters: Effects on Measured Gravimetric Mass in California and in the IMPROVE Network, Journal of the Air & Waste Management Association, 54, 93–104, https://doi.org/10.1080/10473289.2004.10470878, 2004.

Bates, K. H. and Jacob, D. J.: A new model mechanism for atmospheric oxidation of isoprene: global effects on oxidants, nitrogen oxides, organic products, and secondary organic aerosol, Atmospheric Chemistry and Physics, 19, 9613–9640, 2019.

Bekker, C., Walters, W.W., L. T. Murray, and Hastings, M. G.: Nitrate Chemistry in the Northeast US-Part I: Nitrogen Isotopic Seasonality Tracks with Nitrate Formation Chemistry, Atmospheric Chemistry and Physics Discussions, 2023.

Bey, I., Jacob, D. J., Yantosca, R. M., Logan, J. A., Field, B. D., Fiore, A. M., Li, Q., Liu, H. Y., Mickley, L. J., and Schultz, M. G.: Global modeling of tropospheric chemistry with assimilated meteorology: Model description and evaluation, Journal of Geophysical Research: Atmospheres, 106, 23073–23095, 2001.

Breider, T. J., Mickley, L. J., Jacob, D. J., Ge, C., Wang, J., Payer Sulprizio, M., Croft, B., Ridley, D. A., McConnell, J. R., and Sharma, S.: Multidecadal trends in aerosol radiative forcing over the Arctic: Contribution of changes in anthropogenic aerosol to Arctic warming since 1980, Journal of Geophysical Research: Atmospheres, 122, 3573–3594, 2017.

Brenninkmeijer, C. A., Janssen, C., Kaiser, J., Röckmann, T., Rhee, T. S., and Assonov, S. S.: Isotope effects in the chemistry of atmospheric trace compounds, Chemical Reviews, 103, 5125–5162, 2003.

Camargo, J. A. and Alonso, Á.: Ecological and toxicological effects of inorganic nitrogen pollution in aquatic ecosystems: a global assessment, Environment international, 32, 831–849, 2006.

Carter, T. (Tess) S., Joyce, E. E., and Hastings, M. G.: Quantifying Nitrate Formation Pathways in the Equatorial Pacific Atmosphere from the GEOTRACES Peru-Tahiti Transect, ACS Earth and Space Chemistry, 5, 2638–2651, 2021.

Casciotti, K. L., Sigman, D. M., Hastings, M. G., Böhlke, J. K., and Hilkert, A.: Measurement of the oxygen isotopic composition of nitrate in seawater and freshwater using the denitrifier method, Analytical chemistry, 74, 4905–4912, 2002.

CASTNET (Clean Air Status and Trends Network), Retrieved from United States Environmental Protection Agency, available at https://www.epa.gov/castnet, 2019

Crutzen, P. J.: The role of NO and NO_2 in the chemistry of the troposphere and stratosphere, Annual review of earth and planetary sciences, 7, 443–472, 1979.

Dubey, M. K., Mohrschladt, R., Donahue, N. M., and Anderson, J. G.: Isotope specific kinetics of hydroxyl radical (OH) with water (H_2O): Testing models of reactivity and atmospheric fractionation, The Journal of Physical Chemistry A, 101, 1494–1500, 1997.

Elliott, E. M., Kendall, C., Boyer, E. W., Burns, D. A., Lear, G. G., Golden, H. E., Harlin, K., Bytnerowicz, A., Butler, T. J., and Glatz, R.: Dual nitrate isotopes in dry deposition: Utility for partitioning NO_x source contributions to landscape nitrogen deposition, Journal of Geophysical Research: Biogeosciences, 114, 2009.

Fang, H., Walters, W. W., Mase, D., and Michalski, G.: i_NRACM: incorporating ^{15}N into the Regional Atmospheric Chemistry Mechanism (RACM) for assessing the role photochemistry plays in controlling the isotopic composition of NO_x, NO_y, and atmospheric nitrate, Geoscientific Model Development, 14, 5001–5022, 2021.

Fountoukis, C. and Nenes, A.: ISORROPIA II: a computationally efficient thermodynamic equilibrium model for K^+–Ca^{2+}–Mg^{2+}–NH^{4+}–Na^+–SO_4^{2-}–NO_3^-–Cl^-–H_2O aerosols, Atmospheric Chemistry and Physics, 7, 4639–4659, 2007.

Galloway, J. N., Dentener, F. J., Capone, D. G., Boyer, E. W., Howarth, R. W., Seitzinger, S. P., Asner, G. P., Cleveland, C. C., Green, P. A., and Holland, E. A.: Nitrogen cycles: past, present, and future, Biogeochemistry, 70, 153–226, 2004.

Guenther, A. B., Jiang, X., Heald, C. L., Sakulyanontvittaya, T., Duhl, T. any, Emmons, L. K., and Wang, X.: The Model of Emissions of Gases and Aerosols from Nature version 2.1 (MEGAN2. 1): an extended and updated framework for modeling biogenic emissions, Geoscientific Model Development, 5, 1471–1492, 2012.

Hastings, M. G., Sigman, D. M., and Lipschultz, F.: Isotopic evidence for source changes of nitrate in rain at Bermuda, Journal of Geophysical Research: Atmospheres, 108, 2003.

Heald, C. L., Collett Jr, J. L., Lee, T., Benedict, K. B., Schwandner, F. M., Li, Y., Clarisse, L., Hurtmans, D. R., Van Damme, M., and Clerbaux, C.: Atmospheric ammonia and particulate inorganic nitrogen over the United States, Atmospheric Chemistry and Physics, 12, 10295–10312, 2012.

Hering, S. and Cass, G.: The magnitude of bias in the measurement of $PM_{2.5}$ arising from volatilization of particulate nitrate from Teflon filters, Journal of the Air & Waste Management Association, 49, 725–733, 1999.

Hoesly, R. M., Smith, S. J., Feng, L., Klimont, Z., Janssens-Maenhout, G., Pitkanen, T., Seibert, J. J., Vu, L., Andres, R. J., and Bolt, R. M.: Historical (1750–2014) anthropogenic emissions of reactive gases and aerosols from the Community Emissions Data System (CEDS), Geoscientific Model Development, 11, 369–408, 2018.

Holt, J., Selin, N. E., and Solomon, S.: Changes in inorganic fine particulate matter sensitivities to precursors due to large-scale US emissions reductions, Environmental Science & Technology, 49, 4834–4841, 2015.

Hu, L., Millet, D. B., Baasandorj, M., Griffis, T. J., Turner, P., Helmig, D., Curtis, A. J., and Hueber, J.: Isoprene emissions and impacts over an ecological transition region in the US Upper Midwest inferred from tall tower measurements, Journal of Geophysical Research: Atmospheres, 120, 3553–3571, 2015.

Huang, J. and Jaeglé, L.: Wintertime enhancements of sea salt aerosol in polar regions consistent with a sea ice source from blowing snow, Atmospheric Chemistry and Physics, 17, 3699–3712, 2017.

Hudman, R. C., Moore, N. E., Martin, R. V., Russell, A. R., Mebust, A. K., Valin, L. C., and Cohen, R. C.: A mechanistic model of global soil nitric oxide emissions: implementation and space based-constraints., Atmospheric Chemistry & Physics Discussions, 12, 2012.

Jaeglé, L., Quinn, P. K., Bates, T. S., Alexander, B., and Lin, J.-T.: Global distribution of sea salt aerosols: new constraints from in situ and remote sensing observations, Atmospheric Chemistry and Physics, 11, 3137–3157, 2011.

Jaeglé, L., Shah, V., Thornton, J. A., Lopez-Hilfiker, F. D., Lee, B. H., McDuffie, E. E., Fibiger, D., Brown, S. S., Veres, P., and Sparks, T. L.: Nitrogen oxides emissions, chemistry, deposition, and export over the Northeast United States during the WINTER aircraft campaign, Journal of Geophysical Research: Atmospheres, 123, 12–368, 2018.

Kaiser, J., Hastings, M. G., Houlton, B. Z., Röckmann, T., and Sigman, D. M.: Triple oxygen isotope analysis of nitrate using the denitrifier method and thermal decomposition of N2O, Analytical Chemistry, 79, 599–607, 2007.

Kasibhatla, P., Sherwen, T., Evans, M. J., Carpenter, L. J., Reed, C., Alexander, B., Chen, Q., Sulprizio, M. P., Lee, J. D., and Read, K. A.: Global impact of nitrate photolysis in sea-salt aerosol on NO_x, OH, and O_3 in the marine boundary layer, Atmospheric Chemistry and Physics, 18, 11185–11203, 2018.

Kroopnick, P. and Craig, H.: Atmospheric oxygen: isotopic composition and solubility fractionation, Science, 175, 54–55, 1972.

Liu, H., Jacob, D. J., Bey, I., and Yantosca, R. M.: Constraints from ^{210}Pb and [7]Be on wet deposition and transport in a global three-dimensional chemical tracer model driven by assimilated meteorological fields, Journal of Geophysical Research: Atmospheres, 106, 12109–12128, 2001.

Luo, G., Yu, F., and Moch, J. M.: Further improvement of wet process treatments in GEOS-Chem v12.6.0: impact on global distributions of aerosols and aerosol precursors, Geoscientific Model Development, 13, 2879–2903, 2020.

Luo, G., Yu, F., and Schwab, J.: Revised treatment of wet scavenging processes dramatically improves GEOS-Chem 12.0.0 simulations of surface nitric acid, nitrate, and ammonium over the United States, Geoscientific Model Development, 12, 3439–3447, 2019.

McDuffie, E. E., Smith, S. J., O'Rourke, P., Tibrewal, K., Venkataraman, C., Marais, E. A., Zheng, B., Crippa, M., Brauer, M., and Martin, R. V.: A global anthropogenic emission inventory of atmospheric pollutants from sector- and fuel-specific sources (1970–2017): an application of the Community Emissions Data System (CEDS), Earth System Science Data, 12, 3413–3442, https://doi.org/10.5194/essd-12-3413-2020, 2020.

Michalski, G., Bhattacharya, S. K., and Mase, D. F.: Oxygen isotope dynamics of atmospheric nitrate and its precursor molecules, in: Handbook of environmental isotope geochemistry, Springer, 613–635, 2012.

Michalski, G., Scott, Z., Kabiling, M., and Thiemens, M. H.: First measurements and modeling of $\Delta^{17}O$ in atmospheric nitrate, Geophysical Research Letters, 30, 2003.

Millet, D. B., Guenther, A., Siegel, D. A., Nelson, N. B., Singh, H. B., de Gouw, J. A., Warneke, C., Williams, J., Eerdekens, G., Sinha, V., Karl, T., Flocke, F., Apel, E., Riemer, D. D., Palmer, P. I., and Barkley, M.: Global atmospheric budget of acetaldehyde: 3-D model analysis and constraints from in-situ and satellite observations, Atmospheric Chemistry and Physics, 10, 3405–3425, https://doi.org/10.5194/acp-10-3405-2010, 2010.

Morin, S., Sander, R., and Savarino, J.: Simulation of the diurnal variations of the oxygen isotope anomaly (Δ^{17}O) of reactive atmospheric species, Atmospheric Chemistry and Physics, 11, 3653–3671, 2011.

Murray, L. T., Jacob, D. J., Logan, J. A., Hudman, R. C., and Koshak, W. J.: Optimized regional and interannual variability of lightning in a global chemical transport model constrained by LIS/OTD satellite data, Journal of Geophysical Research: Atmospheres, 117, 2012.

NEI (National Emissions Inventory): Retrieved from United States Environmental Protection Agency, available at https://www.epa.gov/air-emissions-inventories/national-emissions-inventory-nei, 2017.

Ridley, D. A., Heald, C. L., and Ford, B.: North African dust export and deposition: A satellite and model perspective, Journal of Geophysical Research: Atmospheres, 117, 2012.

Savard, M. M., Cole, A. S., Vet, R., and Smirnoff, A.: The Δ^{17}O and δ^{18}O values of atmospheric nitrates simultaneously collected downwind of anthropogenic sources–implications for polluted air masses, Atmospheric Chemistry and Physics, 18, 10373–10389, 2018.

Savarino, J., Kaiser, J., Morin, S., Sigman, D. M., and Thiemens, M. H.: Nitrogen and oxygen isotopic constraints on the origin of atmospheric nitrate in coastal Antarctica, Atmospheric Chemistry and Physics, 7, 1925–1945, 2007.

Schlesinger, R. B.: The health impact of common inorganic components of fine particulate matter (PM2. 5) in ambient air: a critical review, Inhalation toxicology, 19, 811–832, 2007.

Shah, V., Jaeglé, L., Thornton, J. A., Lopez-Hilfiker, F. D., Lee, B. H., Schroder, J. C., Campuzano-Jost, P., Jimenez, J. L., Guo, H., and Sullivan, A. P.: Chemical feedbacks weaken the wintertime response of particulate sulfate and nitrate to emissions reductions over the eastern United States, Proceedings of the National Academy of Sciences, 115, 8110–8115, 2018.

Sickles Ii, J. E. and Shadwick, D. S.: Air quality and atmospheric deposition in the eastern US: 20 years of change, Atmospheric Chemistry and Physics, 15, 173–197, 2015.

Sigman, D. M., Casciotti, K. L., Andreani, M., Barford, C., Galanter, M., and Böhlke, J. K.: A bacterial method for the nitrogen isotopic analysis of nitrate in seawater and freshwater, Analytical chemistry, 73, 4145–4153, 2001.

Tai, A. P., Mickley, L. J., and Jacob, D. J.: Correlations between fine particulate matter ($PM_{2.5}$) and meteorological variables in the United States: Implications for the sensitivity of $PM_{2.5}$ to climate change, Atmospheric environment, 44, 3976–3984, 2010.

Thiemens, M. H.: History and applications of mass-independent isotope effects, Annu. Rev. Earth Planet. Sci., 34, 217–262, 2006.

713 US EPA (Environmental Protection Agency): Our nation's air, available at
714 https://gispub.epa.gov/air/trendsreport/ 2017/, 2017.

715 van der Werf, G. R., Randerson, J. T., Giglio, L., van Leeuwen, T. T., Chen, Y., Rogers, B. M.,
716 Mu, M., van Marle, M. J. E., Morton, D. C., Collatz, G. J., Yokelson, R. J., and Kasibhatla, P.
717 S.: Global fire emissions estimates during 1997–2016, Earth System Science Data, 9, 697–720,
718 https://doi.org/10.5194/essd-9-697-2017, 2017.

719 Vicars, W. C. and Savarino, J.: Quantitative constraints on the ^{17}O-excess (Δ^{17}O) signature of
720 surface ozone: Ambient measurements from 50°N to 50°S using the nitrite-coated filter
721 technique, Geochimica et Cosmochimica Acta, 135, 270–287, 2014.

722 Vicars, W. C., Bhattacharya, S. K., Erbland, J., and Savarino, J.: Measurement of the ^{17}O-excess
723 (Δ^{17}O) of tropospheric ozone using a nitrite-coated filter, Rapid Communications in Mass
724 Spectrometry, 26, 1219–1231, 2012.

725 Vicars, W. C., Morin, S., Savarino, J., Wagner, N. L., Erbland, J., Vince, E., Martins, J. M. F.,
726 Lerner, B. M., Quinn, P. K., and Coffman, D. J.: Spatial and diurnal variability in reactive
727 nitrogen oxide chemistry as reflected in the isotopic composition of atmospheric nitrate:
728 Results from the CalNex 2010 field study, Journal of Geophysical Research: Atmospheres,
729 118, 10–567, 2013.

730 Walker, J. M., Philip, S., Martin, R. V., and Seinfeld, J. H.: Simulation of nitrate, sulfate, and
731 ammonium aerosols over the United States, Atmospheric Chemistry and Physics, 12, 11213–
732 11227, 2012.

733 Walker, J. T., Beachley, G., Amos, H. M., Baron, J. S., Bash, J., Baumgardner, R., Bell, M. D.,
734 Benedict, K. B., Chen, X., and Clow, D. W.: Toward the improvement of total nitrogen
735 deposition budgets in the United States, Science of the Total Environment, 691, 1328–1352,
736 2019.

737 Walters, W. W. and Michalski, G.: Theoretical calculation of oxygen equilibrium isotope
738 fractionation factors involving various NO_y molecules, OH, and H_2O and its implications for
739 isotope variations in atmospheric nitrate, Geochimica et Cosmochimica Acta, 191, 89–101,
740 2016.

741 Walters, W. W., Fang, H., and Michalski, G.: Summertime diurnal variations in the isotopic
742 composition of atmospheric nitrogen dioxide at a small midwestern United States city,
743 Atmospheric Environment, 179, 1–11, 2018.

744 Walters, W. W., Michalski, G., Böhlke, J. K., Alexander, B., Savarino, J., and Thiemens, M. H.:
745 Assessing the seasonal dynamics of nitrate and sulfate aerosols at the South Pole utilizing
746 stable isotopes, Journal of Geophysical Research: Atmospheres, 124, 8161–8177, 2019.

747 Wang, X., Jacob, D. J., Downs, W., Zhai, S., Zhu, L., Shah, V., Holmes, C. D., Sherwen, T.,
748 Alexander, B., and Evans, M. J.: Global tropospheric halogen (Cl, Br, I) chemistry and its
749 impact on oxidants, Atmospheric Chemistry and Physics, 21, 13973–13996, 2021.

750 Wesely, M. L. and Lesht, B. M.: Comparison of RADM dry deposition algorithms with a site-
751 specific method for inferring dry deposition, Water, Air, and Soil Pollution, 44, 273–293, 1989.

752 Zhang, L., Jacob, D. J., Knipping, E. M., Kumar, N., Munger, J. W., Carouge, C. C., Van
753   Donkelaar, A., Wang, Y. X., and Chen, D.: Nitrogen deposition to the United States:
754   distribution, sources, and processes, Atmospheric Chemistry and Physics, 12, 4539–4554,
755   2012.

756
757
758
759
760
761
762
763
764
765
766
767
768
769
770
771
772
773
774
775
776
777
778
779
780
781
782
783
784
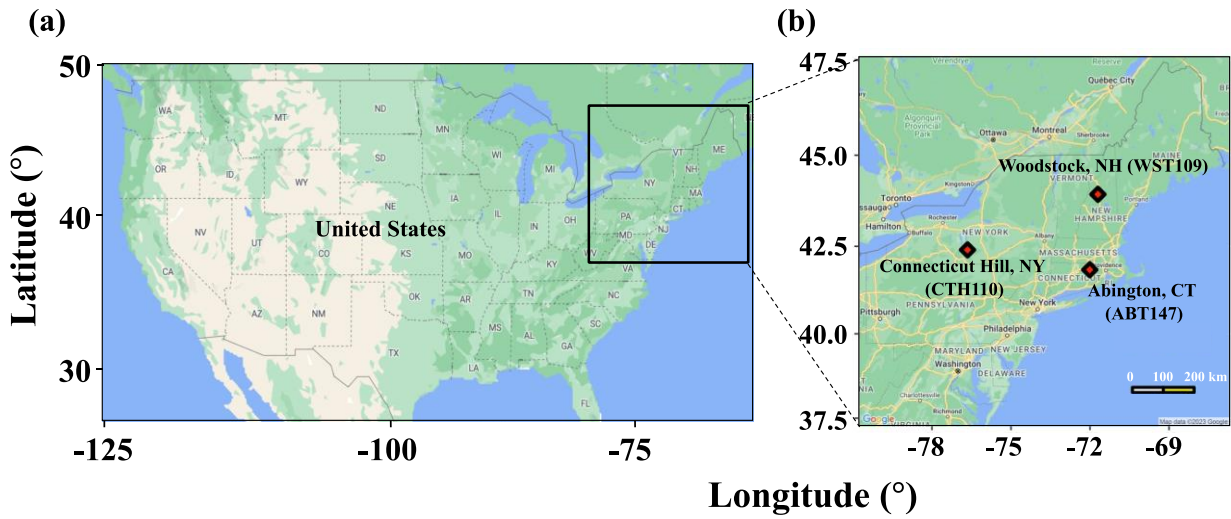
Figure 1. **Map of the United States (a) and selected CASTNET sites (b) for this study in the northeastern US. Major cities (urban areas), transportation routes, and CASTNET sites are also indicated in (b). The image was created using Google Earth (©2023 Google).**

(a) HNO₃
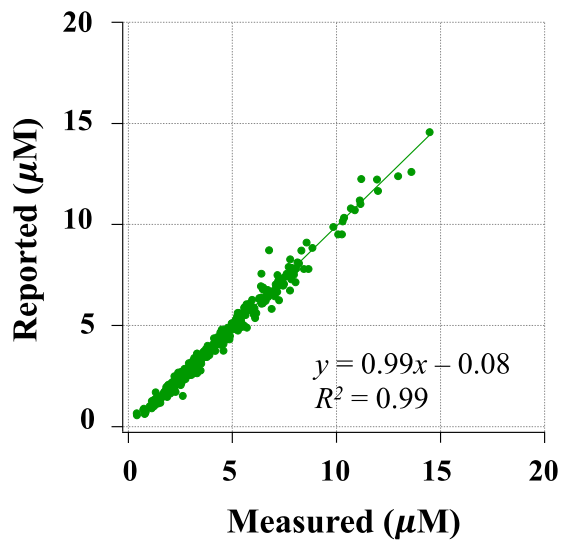
(b) pNO₃
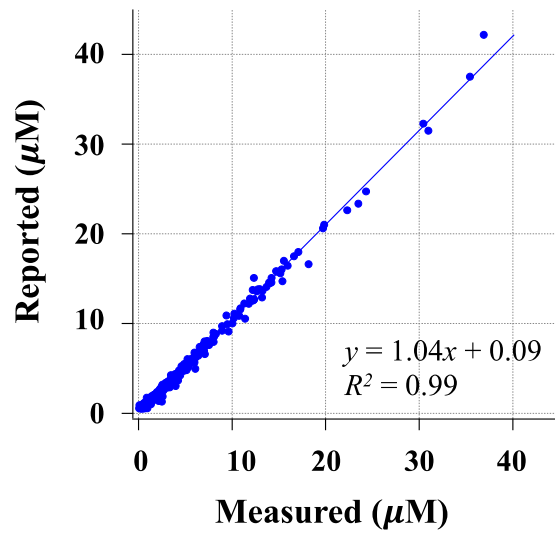
800

801   **Figure 2. Relationship of HNO₃ (a) and pNO₃ (b) filter extract concentrations reported by**

802   **CASTNET and re-measured at Brown University.**

803

804

805
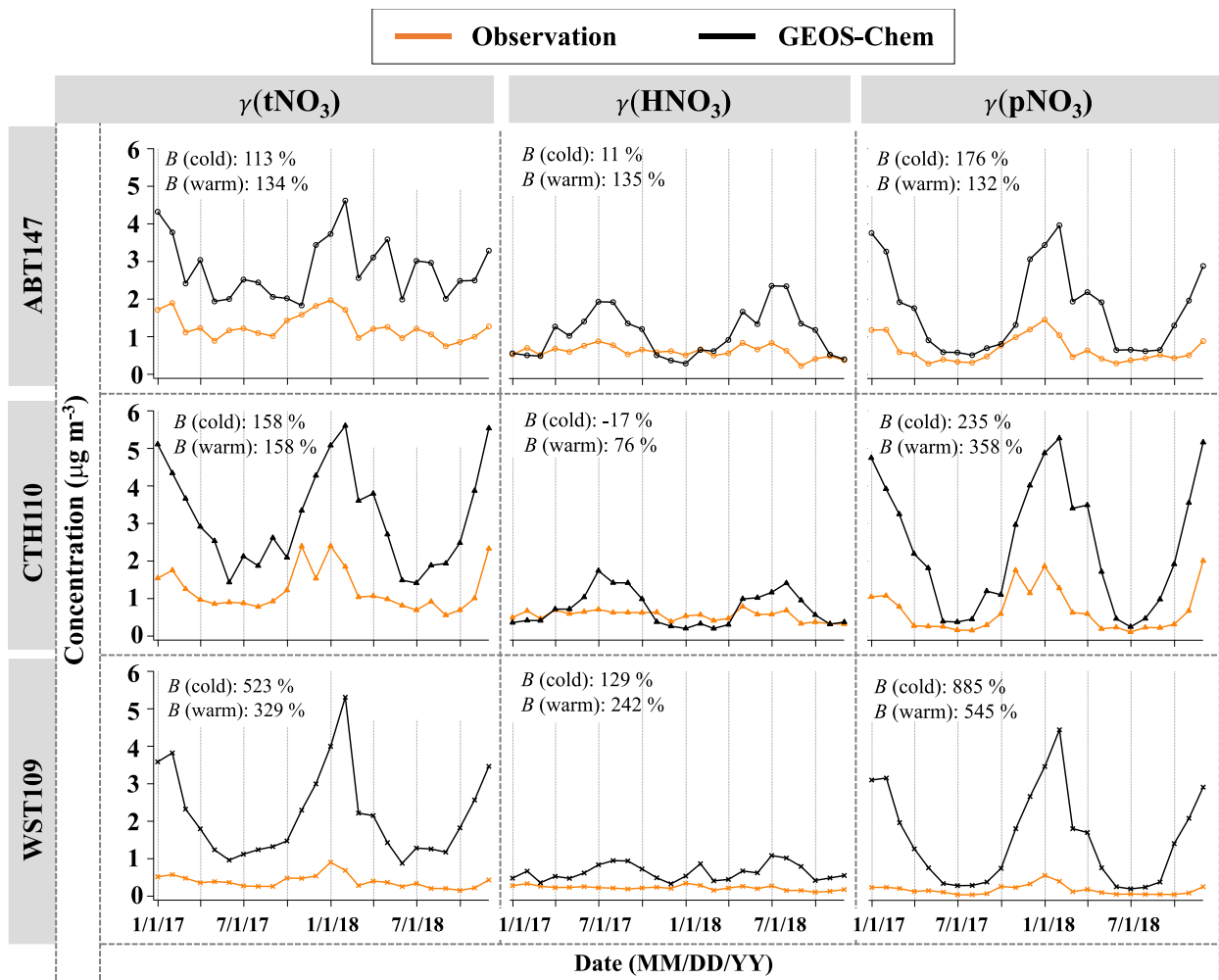
Figure 3. Time series of monthly mean total nitrate, HNO₃, and pNO₃ concentrations (γ) observed and simulated at ABT147, CTH110, and WST109 CASTNET sites. *B* refers to the normalized mean bias for comparison of the model to observations (see section 2.3 in Methods).
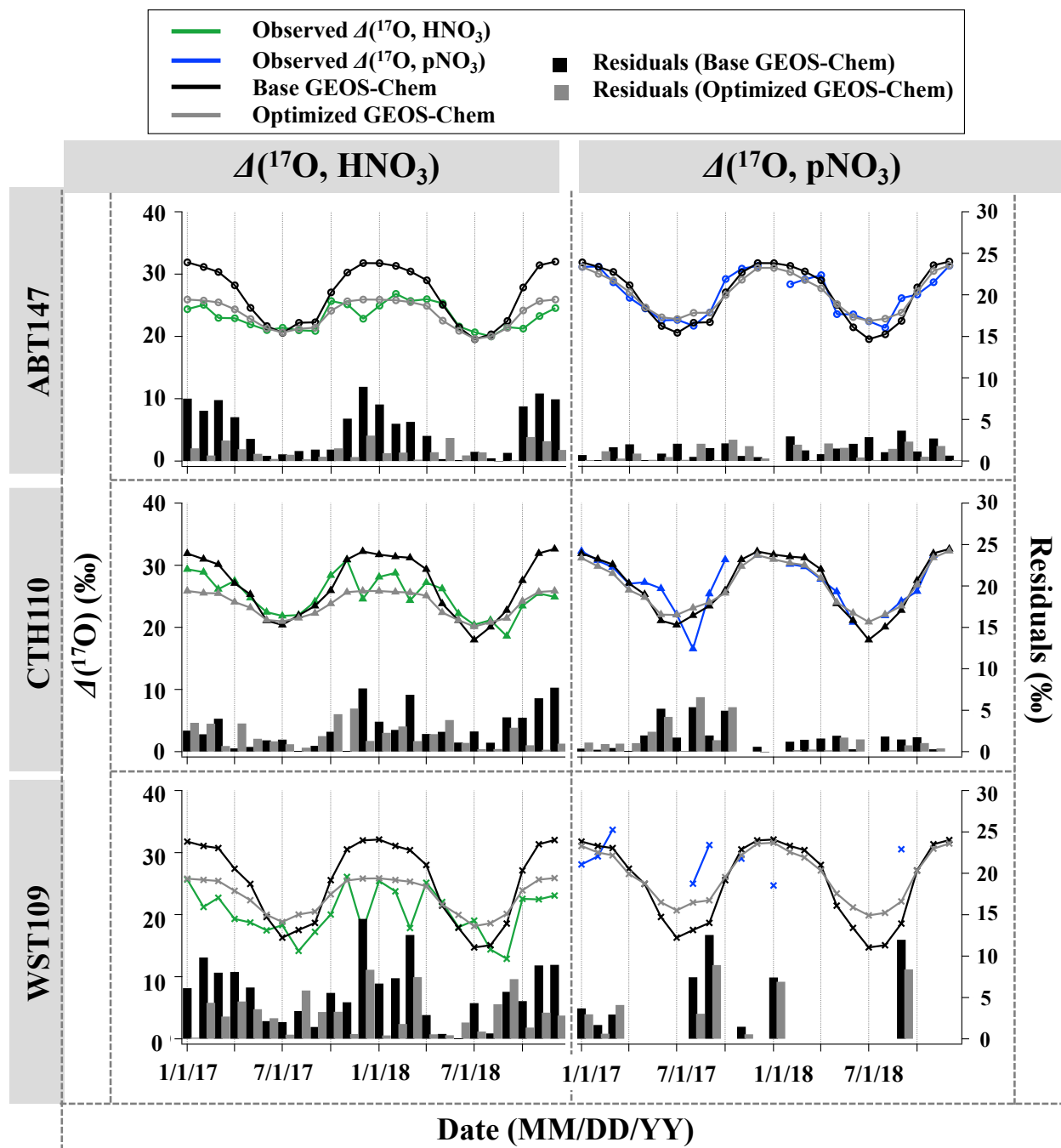
Figure 4. Time series of the monthly mean for observed and calculated $\Delta(^{17}O)$ for HNO₃ and pNO₃ over ABT147, CTH110, and WST109 CASTNET sites. Calculated $\Delta(^{17}O)$ using base (black) and optimized (grey) GEOS-Chem are shown in the plot together. Bars indicate the residuals between calculation and observation.
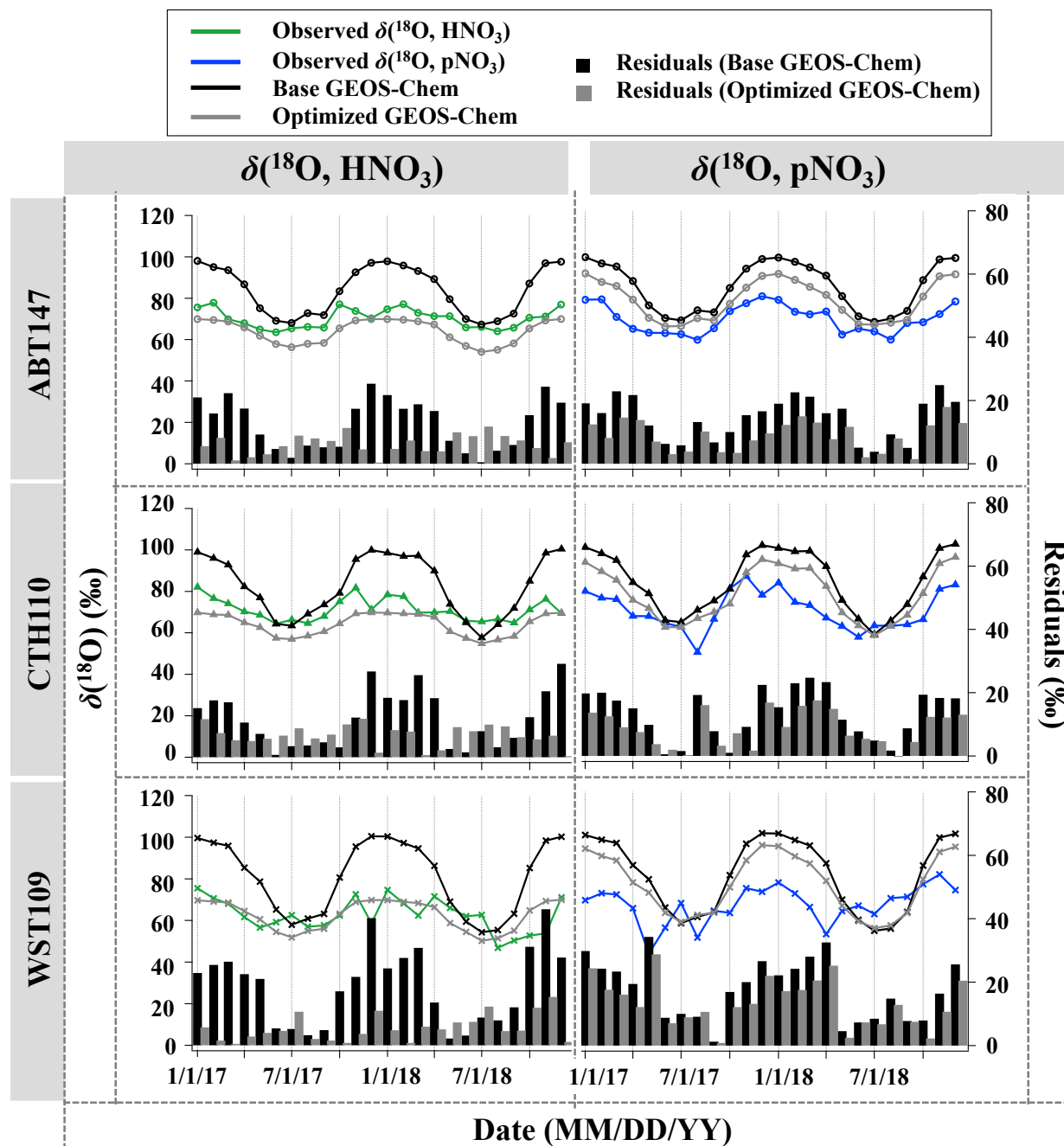
Figure 5. Time series of the monthly mean for observed and calculated $\delta(^{18}O)$ for HNO₃ and pNO₃ over ABT147, CTH110, and WST109 CASTNET sites. Calculated $\delta(^{18}O)$ using base (black) and optimized (grey) GEOS-Chem are shown in the plot together. Bars indicate the residuals between calculation and observation.

832
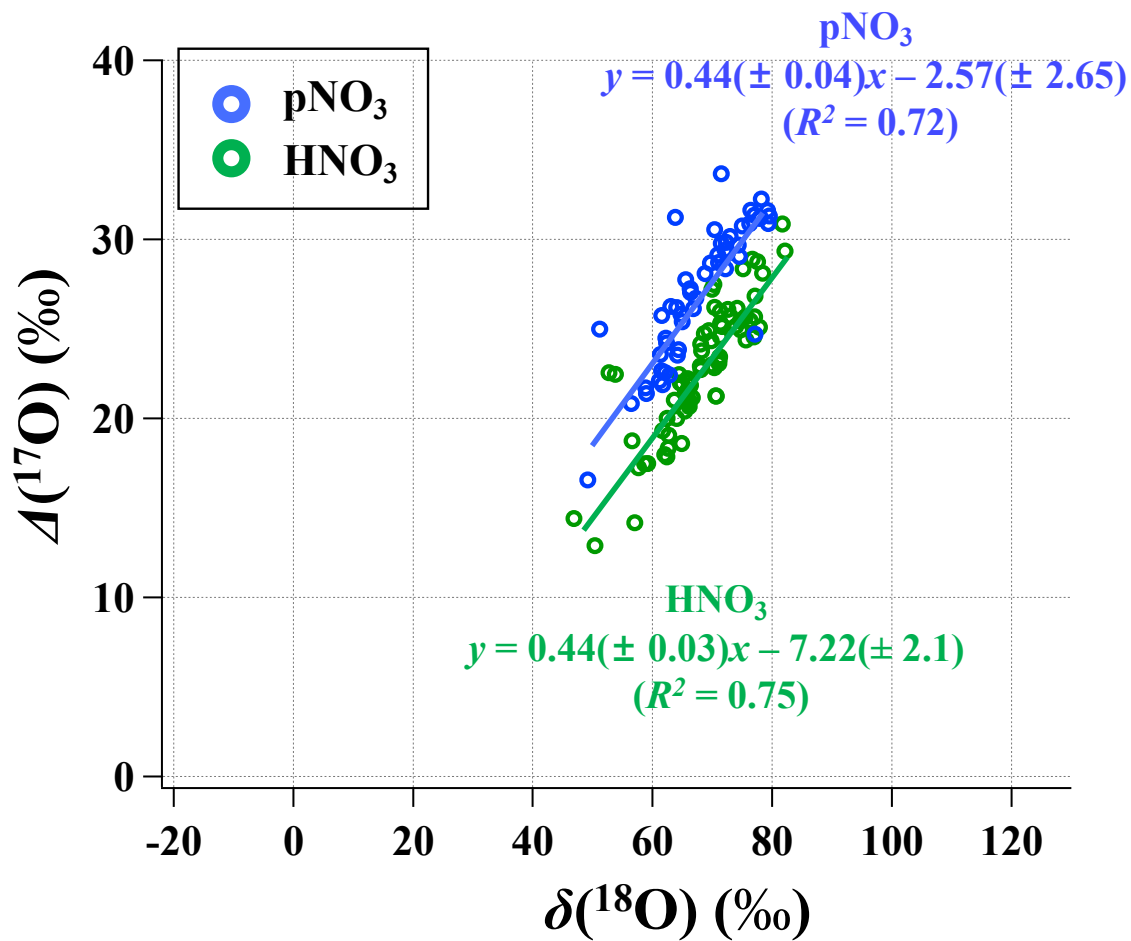
Figure 6. Relationship between the monthly mean ($\delta(^{18}O)$ and $\Delta(^{17}O)$) for observed HNO$_3$

(green) and pNO$_3$ (blue) across all CASTNET sites with correlation coefficient (R^2) and slope

835

836

837

838

839

840

841
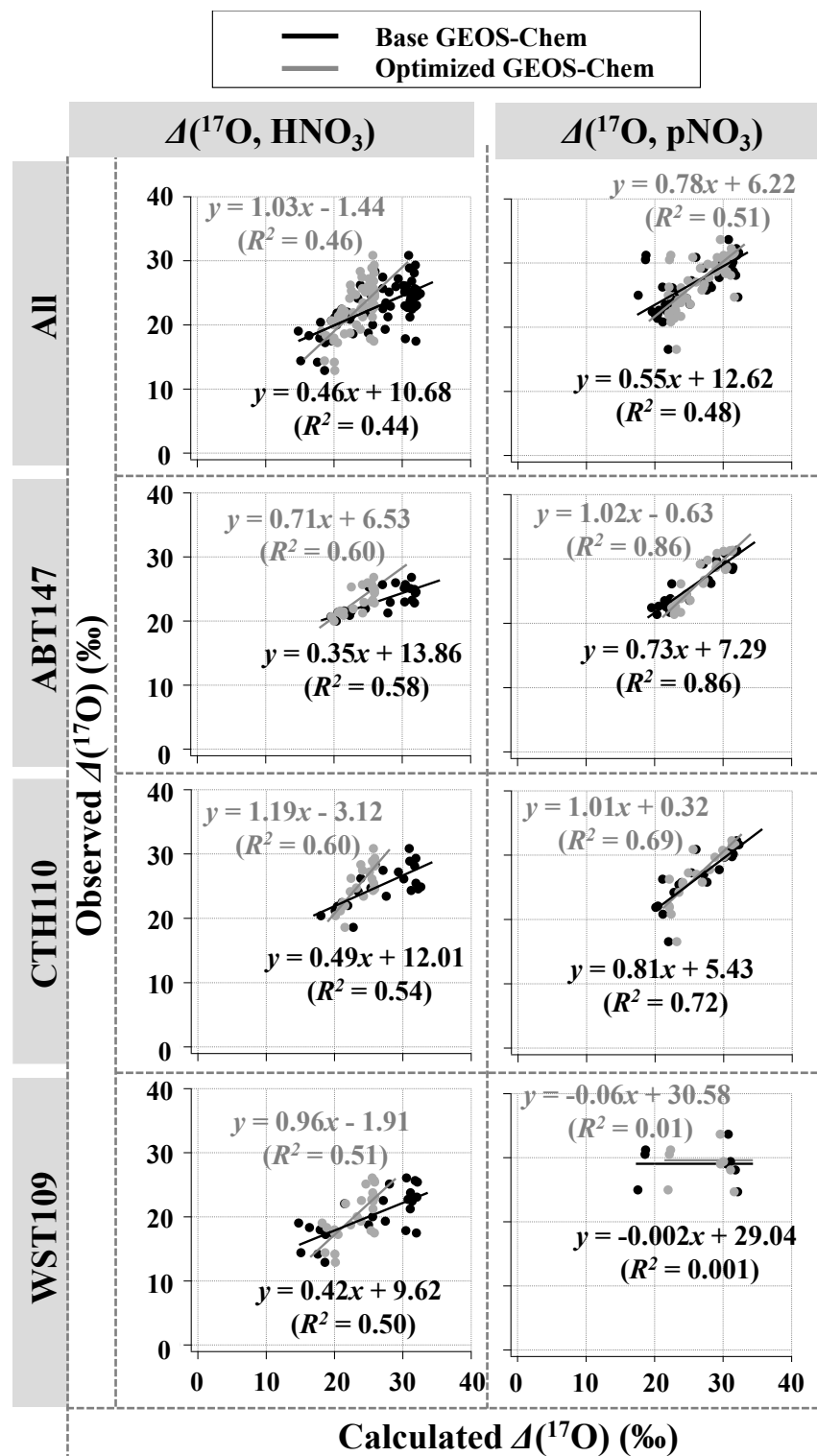
Figure 7. Correlation between observed and calculated $\Delta(^{17}O)$ for HNO$_3$ and pNO$_3$ using base GEOS-Chem (black) and optimized GEOS-Chem (grey) by each site.

844

845

846
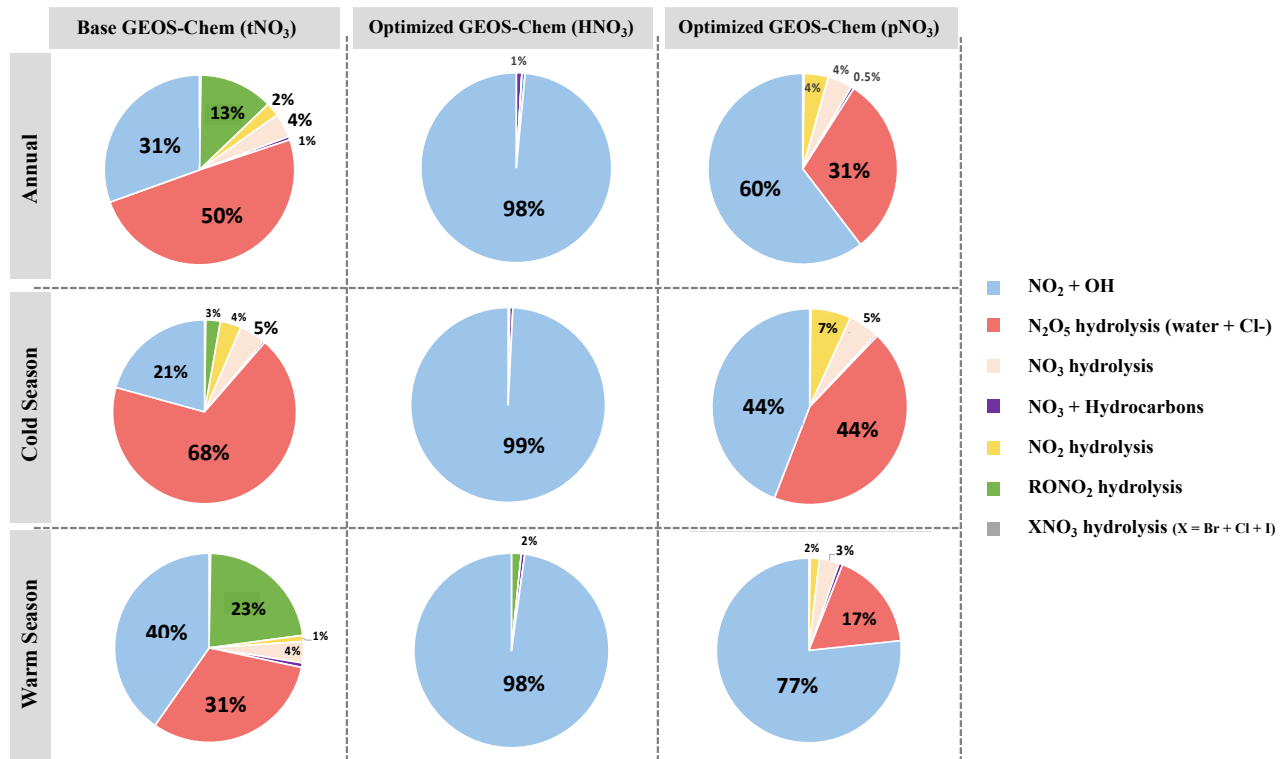
Figure 8. Relative proportions for major nitrate production pathways by season from base GEOS-Chem output (HNO₃ + pNO₃), optimized GEOS-Chem for HNO₃ production only, and optimized GEOS-Chem for pNO₃ production only based on comparison with observations across the three CASTNET sites. Annual refers to the full two-year record (Dec 2016-Dec 2018). The cold and warm seasons refer to Oct-Mar and Apr-Sep, respectively.

852

853
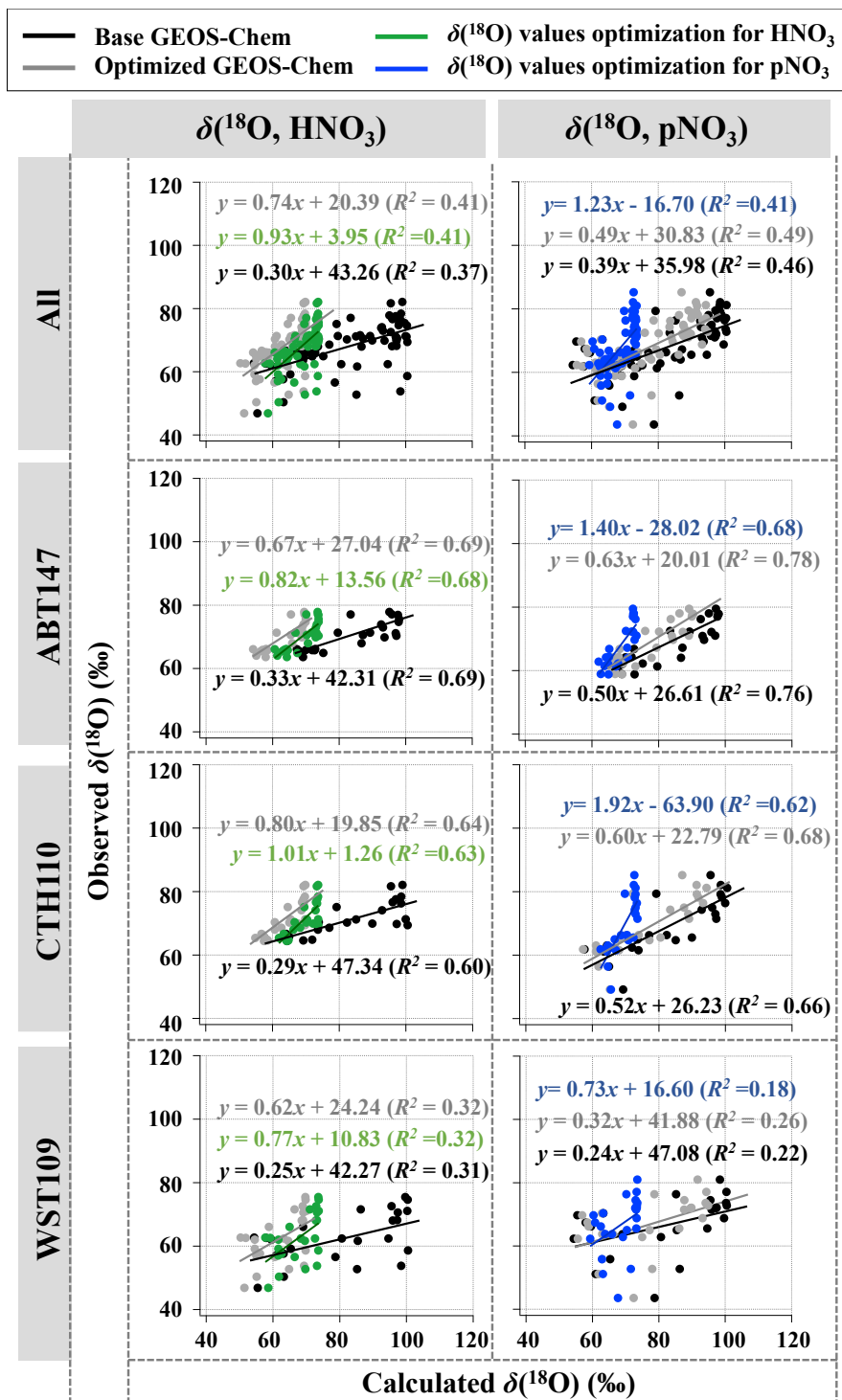
Figure 9. Correlation between observed and calculated $\delta(^{18}O)$ for HNO3 and pNO3 by each site. Calculated $\delta(^{18}O)$ values using base GEOS-Chem, optimized GEOS-Chem, and optimized $\delta(^{18}O)$ values indicated as black, grey, and green (for HNO3) or blue (for pNO3), respectively.

859
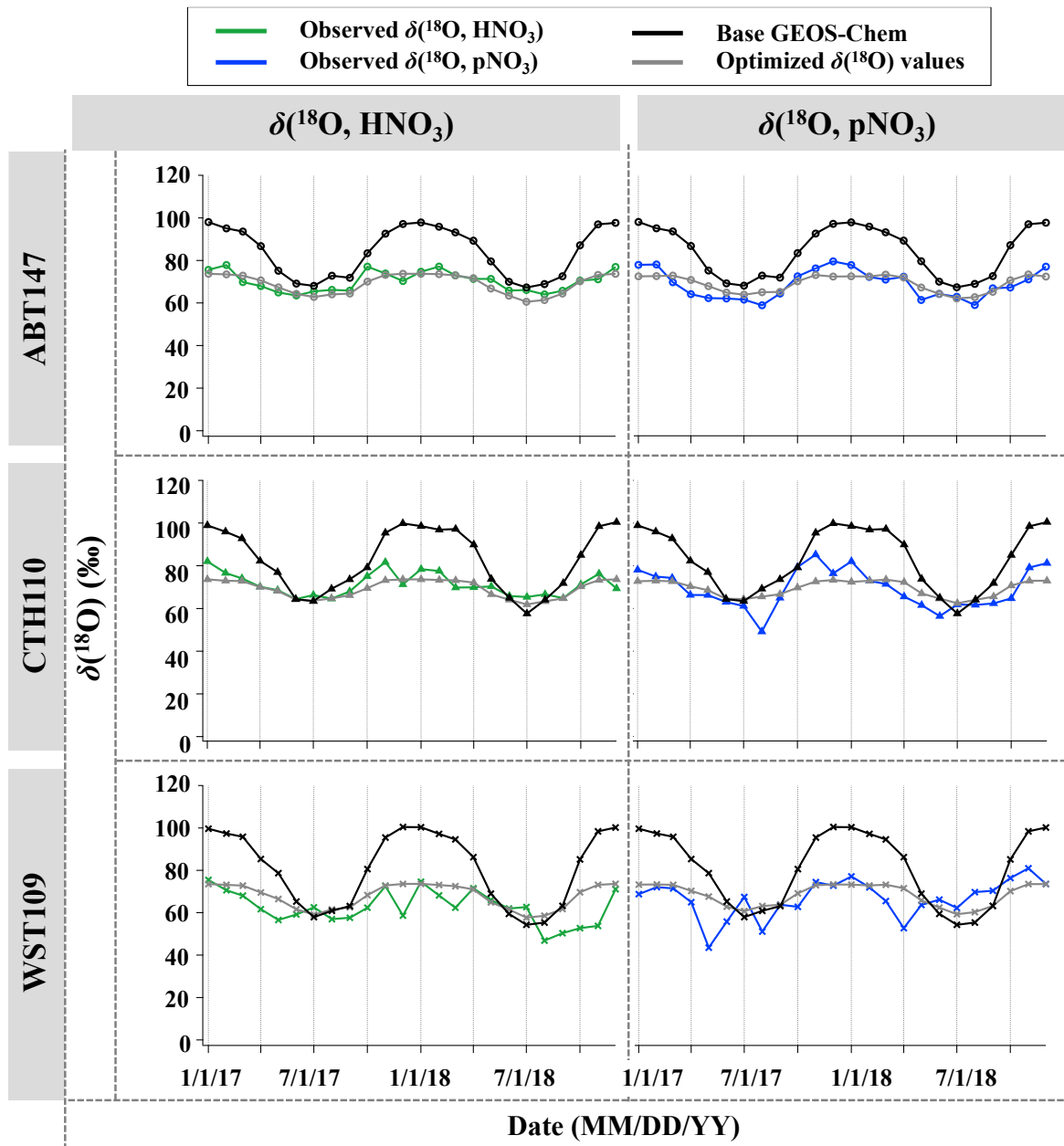
861 **Figure 10. Time series of observed and calculated $\delta(^{18}O)$ for HNO₃ and pNO₃ for ABT147,**

862 **CTH110, and WST109 sites. Calculated $\delta(^{18}O)$ using base GEOS-Chem (black) and using**

863 **optimized $\delta(^{18}O)$ values (grey) are shown in the plot together.**

864

865

866

Table 1. Equations for $\delta(^{18}O)$ and $\Delta(^{17}O)$ calculations by different nitrate formation pathways.

Gas-phase reactions	$\Delta(^{17}O, tNO_3)$	$\delta(^{18}O, tNO_3)$
$NO_2 + OH$	$\frac{2}{3}A\Delta(^{17}O, O_3^*)$	$\frac{2}{3}\delta(^{18}O, NO_2) + \frac{1}{3}\delta(^{18}O, OH)$
NO_3 + Hydrocarbons	$\left(\frac{2}{3}A+\frac{1}{3}\right)\Delta(^{17}O, O_3^*)$	$\frac{2}{3}\delta(^{18}O, NO_2) + \frac{1}{3}\delta(^{18}O, O_3^*)$
Heterogeneous reactions		
N_2O_5 hydrolysis (water + Cl^-)	$\left(\frac{2}{3}A+\frac{1}{6}\right)\Delta(^{17}O, O_3^*)$	$\frac{4}{6}\delta(^{18}O, NO_2) + \frac{1}{6}\delta(^{18}O, O_3^*) + \frac{1}{6}\delta(^{18}O, H_2O)$
NO_3 hydrolysis	$\left(\frac{2}{3}A+\frac{1}{3}\right)\Delta(^{17}O, O_3^*)$	$\frac{2}{3}\delta(^{18}O, NO_2) + \frac{1}{3}\delta(^{18}O, O_3^*)$
NO_2 hydrolysis	$\left(\frac{2}{3}A+\frac{1}{3}\right)\Delta(^{17}O, O_3^*)$	$\frac{2}{3}\delta(^{18}O, NO_2) + \frac{1}{3}\delta(^{18}O, H_2O)$
$RONO_2$ hydrolysis	$\frac{1}{3}A\,\Delta(^{17}O, O_3^*)$	$\frac{2}{3}\delta(^{18}O, NO_2) + \frac{1}{3}\delta(^{18}O, NO_2)$
XNO_3 hydrolysis (X = Br + Cl + I)	$\left(\frac{2}{3}A+\frac{1}{3}\right)\Delta(^{17}O, O_3^*)$	$\frac{2}{3}\delta(^{18}O, NO_2) + \frac{1}{3}\delta(^{18}O, O_3^*)$

Table 2. Summary of the residuals between observed and calculated oxygen isotope deltas by season using the base and optimized GEOS-Chem, respectively.

Residuals		$\Delta(^{17}O, HNO_3)$	$\Delta(^{17}O, pNO_3)$	$\delta(^{18}O, HNO_3)$	$\delta(^{18}O, pNO_3)$
Base GEOS-Chem	Annual	4.1 ‰	2.3 ‰	15.5 ‰	15.9 ‰
	Cold	6.2 ‰	1.7 ‰	23.1 ‰	20.4 ‰
	Warm	2.0 ‰	2.8 ‰	7.9 ‰	11.4 ‰
Optimized GEOS-Chem	Annual	2.0 ‰	1.7 ‰	6.2 ‰	10.4 ‰
	Cold	2.3 ‰	1.4 ‰	5.7 ‰	13.2 ‰
	Warm	1.8 ‰	2.0 ‰	6.7 ‰	7.7 ‰

914 **Table 3. $\delta(^{18}O)$ values for each oxidant before and after optimization based on different**

915 **scenarios**

Atmospheric Oxidants	Assumed $\delta^{18}O$ (‰)	Optimized $\delta^{18}O$ (‰)			
		Non-fixed	Fixed O_3^*	Fixed O_3^* and H_2O	Fixed O_3^*, H_2O, and O_2
O_3^*	126.3	89.9	–	–	–
H_2O	-6.0	-6.5	-180.7	–	–
$O_2/RO_2/HO_2$	23.0	11.1	40.9	44.4	–
OH	-43.0	42.2	-31.3	-39.4	-36

916

917